Atmos. Meas. Tech. Discuss., https://doi.org/10.5194/amt-2018-34
Manuscript under review for journal Atmos. Meas. Tech.
Discussion started: 7 March 2018


Atmospheric Measurement Techniques Discussions

# Improved aerosol correction for OMI tropospheric $NO_2$ retrieval over East Asia: constraint from CALIOP aerosol vertical profile

Mengyao Liu[1,2], Jintai Lin[1], K. Folkert Boersma[2,3], Gaia Pinardi[4], Yang Wang[5], Julien Chimot[6], Thomas Wagner[5], Pinhua Xie[7,8,9], Henk Eskes[2], Michel Van Roozendael[4], François Hendrick[4], Pucai Wang[10], Yingying Yan[1]

1, Laboratory for Climate and Ocean-Atmosphere Studies, Department of Atmospheric and Oceanic Sciences, School of Physics, Peking University, Beijing, China

2, Royal Netherlands Meteorological Institute, De Bilt, the Netherlands

3, Meteorology and Air Quality department, Wageningen University, Wageningen, the Netherlands

4, Royal Belgian Institute for Space Aeronomy (BIRA-IASB), Brussels, Belgium

5, Max Planck Institute for Chemistry, Mainz, Germany

6, Department of Geoscience and Remote Sensing (GRS), Civil Engineering and Geosciences, TU Delft, the Netherlands

7, Anhui Institute of Optics and Fine Mechanics, Key laboratory of Environmental Optics and Technology, Chinese Academy of Sciences, Hefei, China

8, CAS Center for Excellence in Urban Atmospheric Environment, Institute of Urban Environment, Chinese Academy of Sciences, Xiamen, China

9, School of Environmental Science and Optoelectronic Technology, University of Science and Technology of China, Hefei, China

10, IAP/CAS, Institute of Atmospheric Physics, Chinese Academy of Sciences, Beijing, China

Atmos. Meas. Tech. Discuss., https://doi.org/10.5194/amt-2018-34
Manuscript under review for journal Atmos. Meas. Tech.
Discussion started: 7 March 2018


Atmospheric Measurement Techniques Discussions

Correspondent to: Jintai Lin (linjt@pku.edu.cn); K. Folkert Boersma (folkert.boersma@knmi.nl)

**Abstract**

Satellite retrieval of vertical column densities (VCDs) of tropospheric nitrogen dioxide ($NO_2$) is critical for $NO_x$ pollution and impact evaluation. For regions with high aerosol loadings, the retrieval accuracy is greatly affected by whether aerosol optical effects are treated implicitly (as additional "effective" clouds) or explicitly, among other factors. Our previous POMINO algorithm explicitly accounts for aerosol effects to improve the retrieval especially in polluted situations over China, by using aerosol information from GEOS-Chem simulations with further monthly constraint by MODIS/Aqua AOD data. This study updates the retrieval algorithm to POMINO v1.1, by constructing a monthly climatological dataset of aerosol extinction profiles, based on Level-2 CALIOP/CALIPSO data over 2007–2015, to better constrain the modeled aerosol profiles.

We find that GEOS-Chem captures the month-to-month variation of CALIOP aerosol layer height but with a systematic underestimate by about 300–600 m (season and location dependent), due to a too strong vertical gradient of extinction above 1 km. Correcting the model aerosol extinction profiles results in small changes in retrieved cloud fraction, increases in cloud top pressure (within 2–6% in most cases), and increases in tropospheric $NO_2$ VCD by 4–16% over China on a monthly basis in 2012. The improved $NO_2$ VCDs (in POMINO v1.1) are more consistent with independent ground-based MAX-DOAS observations ($R^2$ = 0.80, NMB = -3.4%) than POMINO ($R^2$ = 0.80, NMB = -9.6%) and DOMINO v2 ($R^2$ = 0.68, NMB = -2.1%) are. Especially on haze days, $R^2$ reaches 0.76 for POMINO v1.1, much higher than that for POMINO (0.68) and DOMINO v2 (0.38). Furthermore, the increase in cloud pressure likely reveals a more realistic vertical relationship between cloud and aerosol layers, with aerosols situated above the clouds in certain months instead of always



below the clouds. Our POMINO v1.1 algorithm will be applied to the recently launched TropOMI sensor.

## 1. Introduction

Air pollution is a major environmental problem in China. In particular, China has become the world's largest emitting country of nitrogen oxides ($NO_X$=NO+$NO_2$) due to its rapid economic growth, heavy industries, coal-dominated energy sources, and relatively weak emission control (Cui et al., 2016; Lin et al., 2014a; Stavrakou et al., 2016; Zhang et al., 2009). Tropospheric vertical column densities (VCDs) of nitrogen dioxide ($NO_2$) retrieved from the Ozone Monitoring Instrument (OMI) onboard the Earth

Observing System (EOS) Aura satellite have been widely used to monitor and analyze $NO_X$ pollution over China because of its high spatiotemporal coverage (e.g. Lin et al., 2010; Miyazaki and Eskes, 2013; Verstraeten et al., 2015; Zhao and Wang, 2009). However, $NO_2$ retrieved from OMI and other space-borne instruments are subject to errors in the conversion process from radiance to VCD, particularly with respect to the calculation of tropospheric air mass factor (AMF) that is used to convert tropospheric slant column density to VCD (e.g. Boersma et al., 2011; Bucsela et al., 2013; Lin et al., 2014b, 2015; Lorente et al., 2017). Most current-generation $NO_2$ algorithms do not explicitly account for the effects of aerosols on $NO_2$ AMFs and on prerequisite cloud parameter retrievals. These retrievals often adopt an implicit approach wherein cloud algorithms retrieve "effective cloud" parameters that include the optical effects of aerosols. This implicit method is based on aerosols exerting an effect on the top-of-atmosphere radiance level, whereas the assumed cloud model does not account for the presence of aerosols in the atmosphere (Stammes et al., 2008; Veefkind et al., 2016; Wang et al., 2008b; Wang and Stammes, 2014). In the absence of clouds, an aerosol optical thickness of 1 is then interpreted as an effective cloud fraction of $\pm$0.10, and the value also depends on the aerosol properties (scattering or



absorbing), true surface albedo and geometry angles (Chimot et al., 2016) with an effective cloud pressure closely related to the aerosol layer, at least for aerosols of predominantly scattering nature (e.g. Boersma et al., 2004, 2011, Castellanos et al., 2014, 2015). However, in polluted situations with high aerosol loadings and more absorbing aerosol types, which often occur over China and many other developing regions, the implicit method can result in considerable biases (Castellanos et al., 2014, 2015; Chimot et al., 2016; Kanaya et al., 2014; Lin et al., 2014b).

Lin et al. (2014b, 2015) established the POMINO $NO_2$ algorithm, which builds on the DOMINO v2 algorithm (for OMI $NO_2$ slant columns and stratospheric correction), but improves upon it through a more sophisticated AMF calculation over China. In POMINO, the effects of aerosols on cloud retrievals and $NO_2$ AMFs are explicitly accounted for. In particular, daily information on aerosol optical properties such as aerosol optical depth (AOD), single scattering albedo (SSA), phase function and vertical extinction profiles are taken from nested Asian GEOS-Chem v9-02 simulations. The modeled AOD at 550 nm is further constrained by MODIS/Aqua monthly AOD, with the correction applied to other wavelengths based on modeled aerosol refractive indices (Lin et al., 2014b). However, the POMINO algorithm does not include an observation-based constraint on the vertical profile of aerosols, whose altitude relative to $NO_2$ has strong and complex influences on $NO_2$ retrieval (Castellanos et al., 2015; Leitão et al., 2010; Lin et al., 2014b). This study improves upon the POMINO algorithm by incorporating CALIOP monthly climatology of aerosol vertical extinction profiles to correct for model biases.

The CALIOP lidar, carried on the sun-synchronous CALIPSO satellite, has been acquiring global aerosol extinction profiles since June 2006 (Winker et al., 2010). CALIPSO and Aura are both parts of the National Aeronautics and Space Administration (NASA) A-train constellation of satellites. The overpass time of CALIOP/CALIPSO is only 15 minutes later than OMI/Aura. In spite of issues with



105 the detection limit, radar ratio selection and cloud contamination that cause some
106 biases in CALIOP aerosol extinction vertical profiles (Amiridis et al., 2015; Koffi et
107 al., 2012; Winker et al., 2013), comparisons of aerosol extinction profiles between
108 ground-based lidar and CALIOP show good agreements (Kacenelenbogen et al.,
109 2014; Kim et al., 2009; Misra et al., 2012). However, CALIOP is a nadir-viewing
110 instrument that measures the atmosphere along the satellite ground-track with a
111 narrow field-of-view. This means that the daily geographical coverage of CALIOP is
112 much smaller than that of OMI. Thus previous studies often used monthly/seasonal
113 regional mean CALIOP data to study aerosol vertical distributions or to evaluate
114 model simulations (Chazette et al., 2010; Johnson et al., 2012; Koffi et al., 2012; Ma
115 and Yu, 2014; Sareen et al., 2010). However, the major monthly/seasonal CALIOP
116 data are too coarse in spatial resolution (i.e. NASA's official monthly Level-3
117 CALIOP dataset with spatial resolution 2° long. × 5° lat.) or in temporal resolution
118 (i.e. LIVAS 5-year based 1° × 1° CALIOP dataset).

119 Here we construct a custom monthly climatology of aerosol vertical extinction
120 profiles based on 9-years (2007–2015) worth of CALIOP Version 3 Level-2 532 nm
121 data. On a climatological basis, we use the CALIOP monthly data to adjust
122 GEOS-Chem profile in each grid cell for each day of the same month in any year. We
123 then use the corrected GEOS-Chem vertical extinction profiles in the retrievals of
124 cloud parameters and $NO_2$. Finally, we evaluate our updated POMINO retrieval
125 (hereafter referred to as POMINO v1.1) and the existing POMINO and DOMINO v2
126 retrievals, using ground-based MAX-DOAS $NO_2$ column measurements at three
127 urban/suburban sites in East China for the year of 2012 and several months in
128 2008/2009.

129 Section 2 describes the construction of CALIOP aerosol extinction vertical profile
130 monthly climatology, the POMINO v1.1 retrieval approach, and the MAX-DOAS
131 data. It also presents the criteria for comparing different $NO_2$ retrieval products and



for selecting coincident OMI and MAX-DOAS data. Section 3 compares our CALIOP climatology with NASA's official Level-3 CALIOP dataset and GEOS-Chem simulation results. Sections 4 and 5 compare POMINO v1.1 to POMINO to analyze the influence of improved aerosol vertical profiles on retrievals of cloud parameters and $NO_2$ VCDs, respectively. Section 6 evaluates POMINO, POMINO v1.1 and DOMNO v2 $NO_2$ VCDs using the MAX-DOAS data. Section 7 concludes our study.

## 2. Data and methods

### *2.1 Constructing a CALIOP monthly mean extinction profile climatology*

CALIOP is a dual-wavelength polarization lidar measuring attenuated backscatter radiation at 532 and 1064 nm since June 2006. The vertical resolution of aerosol extinction profiles is 30 m below 8.2 km and 60 m up to 20.2 km (Winker et al., 2013), with a total of 399 sampled altitudes. The horizontal resolution of CALIOP scenes is 335 m along the orbital track and is given over a 5km horizontal resolution in Level-2 data. Here we use the daily all-sky Version 3 CALIOP Level-2 aerosol profile product at 532 nm from 2007 to 2015 to construct a monthly Level-3 climatological dataset of aerosol extinction profiles over China and nearby regions. We choose the all-sky product instead of clear-sky data, since previous studies indicate that the climatological aerosol extinction profiles are affected insignificantly by the presence of clouds (Koffi et al., 2012; Winker et al., 2013). As we use this climatological data to adjust GEOS-Chem results, choosing all-sky data improves consistency with the model simulation when doing the daily correction.

We apply a number of criteria to ensure data quality of each pixel, mainly following Winker et al. (2013) and Amiridis et al. (2015). In brief, only the pixels with Cloud Aerosol Discrimination (CAD) scores between -20 and -100 with extinction Quality Control (QC) flag valued at 0, 1, 18, and 16 are selected. We further discard samples with an extinction uncertainty of 99.9 $km^{-1}$, which is indicative of unreliable retrieval.

Atmos. Meas. Tech. Discuss., https://doi.org/10.5194/amt-2018-34
Manuscript under review for journal Atmos. Meas. Tech.
Discussion started: 7 March 2018




We only accept extinction values falling in the range from 0.0 to 1.25, according to CALIOP observation thresholds. Previous studies showed that weakly scattering edges of icy clouds are sometimes misclassified as aerosols (Winker et al., 2013). To eliminate contamination from icy clouds we exclude the aerosol layers above the cloud layer (with layer-top temperature below 0 ℃) when both of them are above 4km (Winker et al., 2013).

After the pixel-based screening, we aggregate the CALIOP data at the model grid (0.667° long. x 0.5° lat.) and vertical resolution (47 layers, with 36 layers or so in the troposphere). For each grid cell, we choose the CALIOP pixels within 1.5° of the grid cell center. CALIOP Level-2 data are always presented at the fixed 399 altitudes above sea level. To account for the difference in surface elevation between a CALIOP pixel and the respective model grid cell, we convert the altitude of the pixel to a height above the ground, by using the surface elevation data provided in CALIOP. We then average horizontally and vertically the profiles of all pixels within one model grid cell and layer. We do the regridding day-by-day for all grid cells to ensure that GEOS-Chem and CALIOP extinction profiles are coincident spatially and temporally. Finally, we compile a monthly climatological dataset by averaging over 2007–2015. The ratio of climatological monthly CALIOP to monthly GEOS-Chem profiles represents the scaling profile to adjust the daily GEOS-Chem profiles in the same month (see Sect. 2.2).

Figure 1 shows the number of aerosol extinction profiles in each grid cell and 12 x 9 = 108 months that are used to compile the CALIOP climatology, both before and after data screening. Table 1 presents additional information on monthly and yearly bases. On average, there are 165 and 47 aerosol extinction profiles per month per grid cell before and after screening, respectively. In the final 9-year monthly climatology, each grid cell has about 420 aerosol extinction profiles on average, about 28% of the prior-screening profiles. Figure 1 shows that the number of valid profiles decreases

Atmos. Meas. Tech. Discuss., https://doi.org/10.5194/amt-2018-34
Manuscript under review for journal Atmos. Meas. Tech.
Discussion started: 7 March 2018


Atmospheric Measurement Techniques Discussions

185 sharply over the Tibet Plateau and at higher latitudes (> 43 ° N) due to complex
186 terrain and icy/snowy ground.

187 As discussed above, we choose the CALIOP pixels within 1.5° of a grid cell center.
188 We test this choice by examining the aerosol layer height (ALH) produced for that
189 grid cell. The ALH is defined as the extinction-weighted height of aerosols (see Eq. 1,
190 where $n$ denotes the number of tropospheric layers, $\varepsilon_i$ the aerosol extinction at
191 layer $i$, and $H_i$ the layer center height above the ground). We find that choosing
192 pixels within 1.0° of a grid cell center leads to a nosier horizontal distribution of
193 ALH, owing to the small footprint of CALIOP. On the other hand, choosing 2.0°
194 leads to a too smooth spatial gradient of ALH with local characteristics of aerosol
195 vertical distributions are largely lost. We thus decide that 1.5 ° is a good balance
196 between noise and smoothness.

197 $$\mathrm{ALH} = \frac{\sum_{i=1}^{i=n} \varepsilon_i H_i}{\sum_{i=1}^{i=n} \varepsilon_i} \qquad (1)$$

198 Certain grid cells do not contain sufficient valid observations for some months of the
199 climatological dataset. We fill in missing monthly values of a grid cell using valid
200 data in the surrounding 5 x 5 = 25 grid cells (within ~ 100 km). If the 25 grid cells do
201 not have enough valid data (see next paragraph for details), we use those in the
202 surrounding 7 x 7 = 49 grid cells (within ~ 150 km). A similar procedure is used by
203 Lin et al. (2014b, 2015) to fill in missing values in the gridded MODIS AOD dataset.

204 For each grid cell in each month, we further correct singular values in the vertical
205 profile. In a month, if a grid cell *i* has an ALH outside mean $\pm 1\,\sigma$ of its surrounding
206 25 or 49 grid cells, we select *i*'s surrounding grid cell *j* whose ALH is the median of
207 *i*'s surrounding grid cells, and use *j*'s profile to replace *i*'s. Whether 25 or 49
208 surrounding grid cells are chosen depends on the number of valid pixels shown in Fig.
209 1b. If the number of valid pixels in *i* is below mean–1 σ of all grid cells in the whole

Atmos. Meas. Tech. Discuss., https://doi.org/10.5194/amt-2018-34
Manuscript under review for journal Atmos. Meas. Tech.
Discussion started: 7 March 2018


Atmospheric Measurement Techniques Discussions

domain, which is often the case for Tibetan grid cells, we use *i*'s surrounding 49 grid cells; otherwise we use *i*'s surrounding 25 grid cells.

### *2.2 POMINO v1.1 retrieval approach*

The $NO_2$ retrieval consists of three steps. First, the total $NO_2$ slant columns density (SCD) is retrieved using the Differential Optical Absorption Spectroscopy (DOAS) technique (for the 405-465 nm spectral window in the case of OMI). The uncertainty of the SCD is determined by the appropriateness of the fitting technique, the instrument noise, the choice of fitting window, and the orthogonality of the absorbers' cross sections (Bucsela et al., 2006; van Geffen et al., 2015; Lerot et al., 2010; Richter et al., 2011; Zara et al., 2018). The $NO_2$ SCD in DOMINO v2 has a bias at about $0.5 \times 10^{15}$ molec. $cm^{-2}$ (Belmonte Rivas et al., 2014; Dirksen et al., 2011; van Geffen et al., 2015), which can be reduced by improving wavelength calibration and including $O_2$–$O_2$ and liquid water absorption in the fitting model (van Geffen et al., 2015). The tropospheric SCD is then obtained by subtracting the stratospheric SCD from the total SCD. The bias in the total SCD is mostly absorbed by this stratospheric separation step, which will not propagate into the tropospheric SCD (van Geffen et al., 2015). The last step converts the tropospheric SCD to VCD by using the tropospheric AMF (VCD = SCD / AMF). The tropospheric AMF is calculated by using look-up tables (in most retrieval algorithms) or online radiative transfer modeling (in POMINO) driven by ancillary parameters, which act as the dominant source of errors in retrieved $NO_2$ VCD data over polluted areas (Boersma et al., 2007; Lin et al., 2014b, 2015; Lorente et al., 2017).

Our POMINO algorithm focuses on the tropospheric AMF calculation over China and nearly regions, taking the tropospheric SCD (Dirksen et al., 2011) from DOMINO v2 (Boersma et al., 2011). POMINO improves upon the DOMINO v2 algorithm in the treatment of aerosols, surface reflectance, online radiative transfer calculations, spatial resolution of $NO_2$ vertical profile, consistency between cloud and $NO_2$ retrievals, and



other aspects (Lin et al., 2014b, 2015). In brief, we use the parallelized LIDORT-driven AMFv6 package to derive both cloud parameters and tropospheric $NO_2$ AMFs for individual OMI pixels without use of look-up tables. $NO_2$ vertical profiles, aerosol optical properties and aerosol vertical profiles are taken from the nested GEOS-Chem model over Asia (0.667 ° long. × 0.5° lat. before May 2013 and 0.3125 ° long. × 0.25 ° lat. afterwards), and pressure and temperature profiles are taken from the GEOS-5 and GEOS-FP assimilated meteorological fields that drive GEOS-Chem simulations. Model aerosols are further adjusted by satellite data (see below). We adjust the pressure profiles based on the difference in elevation between the pixel center and the matching model grid cell (Zhou et al., 2010). We also account for the effects of surface bidirectional reflectance distribution function (BRDF) (Lin et al., 2014b; Zhou et al., 2010) by taking three kernel parameters (isotropic, volumetric and geometric) from the MODIS MCD43C2 data set at 440 nm (Lucht et al., 2000). As a prerequisite, the cloud retrieval is done through the $O_2$-$O_2$ algorithm (Acarreta et al., 2004; Stammes et al., 2008) with $O_2$-$O_2$ SCD from OMCLDO2, and with pressure, temperature, surface reflectance, aerosols and other ancillary information consistent with the $NO_2$ retrieval.

POMINO uses the temporally and spatially varying aerosol information, including AOD, SSA, phase function and vertical profiles from GEOS-Chem simulations. POMINO v1.1 (this work) further uses CALIOP data to constrain the shape of aerosol vertical extinction profile. We run the model at a resolution of 0.3125° long. × 0.25° lat. before May 2013 and 0.667° long. × 0.5° lat. afterwards, as determined by the resolution of the driving meteorological fields. We then regrid the finer resolution model results to 0.667° long. × 0.5° lat., to be consistent with the CALIOP data grid. We then sample the model data at times and locations with valid CALIOP data at 532nm to establish the model monthly climatology.

Atmos. Meas. Tech. Discuss., https://doi.org/10.5194/amt-2018-34
Manuscript under review for journal Atmos. Meas. Tech.
Discussion started: 7 March 2018


Atmospheric Measurement Techniques Discussions

For any month in a grid cell, we divide the CALIOP monthly climatology of aerosol extinction profile shape by model climatological profile shape to obtain a unitless scaling profile (Eq. 2), and apply this scaling profile to all days of that month in all years (Eq. 3). Such a climatological adjustment is based on the assumption that systematic model limitations are month-dependent and persist over the years and days (e.g., a too strong vertical gradient, see Sect. 3.3).

In Eqs. 2 and 3, $E^{C}$ represents the CALIOP climatological aerosol extinction coefficient, $E^{G}$ the GEOS-Chem extinction, $E^{Gr}$ the post-scaling model extinction, and R the scaling profile. The subscript *i* denotes a grid cell, *k* a vertical layer, *d* a day, *m* a month, and *y* a year. Note that in Eq. 2, the extinction coefficient at each layer is normalized relative to the maximum value of that profile. This procedure ensures that the scaling is based on the relative shape of the extinction profile and is thus independent of the accuracies of CALIOP and GEOS-Chem AOD. We keep the absolute AOD value of GEOS-Chem unchanged in this step.

$$R_{i,k,m} = \frac{E^{C}_{i,k,m}/\max(E^{C}_{i,k,m})}{E^{G}_{i,k,m}/max(E^{G}_{i,k,m})} \quad (2)$$

$$E^{Gr}_{i,k,d,m,y} = E^{G}_{i,k,d,m,y} \times R_{i,k,m} \quad (3)$$

In POMINO, the GEOS-Chem AOD are further constrained by a MODIS/Aqua Collection 5.1 monthly AOD dataset compiled on the model grid (Lin et al., 2014b, 2015). POMINO v1.1 uses the Collection 5.1 AOD data before May 2013 and Collection 6 data afterwards. For adjustment, model AOD are projected to a 0.667° long. × 0.5° lat. grid and then sampled at times and locations with valid MODIS data (Lin et al., 2015). As shown in Eq. 4, $\tau^{M}$ denotes MODIS AOD, $\tau^{G}$ GEOS-Chem AOD, and $\tau^{Gr}$ post-adjustment model AOD. The subscript *i* denotes a grid cell, *d* a day, *m* a month, and *y* a year. This AOD adjustment ensures that in any

Atmos. Meas. Tech. Discuss., https://doi.org/10.5194/amt-2018-34
Manuscript under review for journal Atmos. Meas. Tech.
Discussion started: 7 March 2018


Atmospheric Measurement Techniques Discussions

month, monthly mean GEOS-Chem AOD is the same as MODIS AOD while the modeled day-to-day variability is kept.

$$\tau_{i,d,m,y}^{Gr} = \frac{\tau_{i,m,y}^{M}}{\tau_{i,m,y}^{G}} \times \tau_{i,d,m,y}^{G} \quad (4)$$

Equations 5–6 show the complex effects of aerosols in calculating the AMF for any pixel. The AMF is the linear sum of tropospheric layer contributions to the slant column weighted by the vertical subcolumns (Eq. 5). The box AMF, $amf_k$, describes the sensitivity of $NO_2$ SCD to layer $k$, and $x_{a,k}$ represent the subcolumn of layer $k$ from a priori $NO_2$ profile. The $l$ represent the first integrated layer, which is the layer above the ground for clear sky, or the layer above cloud top for cloudy sky. The $t$ represent the tropopause layer. POMINO assumes the independent pixel approximation (IPA) (Martin, 2002). This means that the calculated AMF for any pixel consists of a fully cloudy-sky portion ($\mathrm{AMF}_{cld}$) and a fully clear-sky portion ($\mathrm{AMF}_{clr}$), with weights based on the cloud radiance fraction (CRF) (Eq. 6). $\mathrm{AMF}_{cld}$ is affected by above-cloud aerosols, and $\mathrm{AMF}_{clr}$ is affected by aerosols in the whole column. Also, aerosols affect the retrieval of CRF. Thus, the improvement of aerosol vertical profile in POMINO v1.1 affects all the three quantities in Eq. 6 and thus leads to complex impacts on retrieved $NO_2$ VCD.

$$\mathrm{AMF} = \frac{\sum_l^t amf_k x_{a,k}}{\sum_l^t x_{a,k}} \quad (5)$$

$$\mathrm{AMF} = \mathrm{AMF}_{cld} \cdot \mathrm{CRF} + \mathrm{AMF}_{clr} \cdot (1 - \mathrm{CRF}) \quad (6)$$

*2.3 OMI pixel selection to evaluate POMINO v1.1, POMINO and DOMINO v2*

We exclude OMI pixels affected by row anomaly (Schenkeveld et al., 2017) or with high albedo caused by icy/snowy ground. To screen out cloudy scenes, we choose pixels with CRF below 50% (effective cloud fraction is typically below 20%) in POMINO.



311 The selection of CRF threshold influences the validity of pixels. The "effective" CRF
312 in DOMINO implicitly includes the influence of aerosols. In POMINO, the aerosol
313 contribution is separated from that of the clouds, resulting in a lower CRF than for
314 DOMINO. The CRF differs insignificantly between POMINO and POMINO v1.1,
315 because the same AOD and other non-aerosol ancillary parameters are used in the
316 retrieval process. Using the CRF from POMINO instead of DOMINO for cloud
317 screening means that the number of "valid" pixels in DOMINO increases by about
318 25%, particularly because much more pixels with high pollutant (aerosol and $NO_2$)
319 loadings are now included. This potentially reduces the sampling bias (Lin et al.,
320 2014b, 2015), but the drawback is that the ensemble of pixels now includes scenes
321 with high "aerosol radiative fractions". Further research is needed to fully
322 understanding how much these high-aerosol scenes may be subject to the same
323 screening issues as the cloudy scenes, although the limited evidence here and in Lin et
324 al. (2014b, 2015) suggests that including these scenes does not affect the accuracy of
325 $NO_2$ retrieval.

326 *2.4 MAX-DOAS data*

327 We use MAX-DOAS measurements at three suburban or urban sites in East China,
328 including one urban site at the Institute of Atmospheric Physics (IAP) in Beijing
329 (116.38° E, 39.38 ° N), one suburban site in Xianghe County (116.96° E, 39.75 ° N)
330 to the south of Beijing, and one urban site in the Wuxi City (120.31° E, 31.57 ° N) in
331 the Yangzi River delta (YRD). Figure 2 shows the locations of these sites overlaid
332 with POMINO v1.1 $NO_2$ VCDs in August 2012. Table 2 summarizes the information
333 of MAX-DOAS measurements.

334 The instruments in IAP and in Xianghe were designed at BIRA-IASB (Clémer et al.,
335 2010). Such an instrument is a dual-channel system composed of two thermally
336 regulated grating spectrometers, covering the ultraviolet (300–390 nm) and visible
337 (400–720 nm) wavelengths. It measures scattered sunlight every 15 minutes at nine



338 elevation angles: 2°, 4°, 6°, 8°, 10°, 12°, 15°, 30°, and 90°. The
339 telescope of the instrument is pointed to the north. The data are analyzed following
340 Hendrick et al. (2014). The Xianghe suburban site is influenced by pollution from the
341 surrounding major cities like Beijing and Tianjin. At Xianghe, MAX-DOAS data are
342 data are continuously available since early 2011, and data in 2012 are used here for
343 comparison with OMI products. At IAP, MAX-DOAS data are available in 2008 and
344 2009 (Table 2), thus for comparison purposes we process OMI products to match the
345 MAX-DOAS times.

346 Located on the roof of an 11-story building, the instrument at Wuxi was developed by
347 Anhui Institute of Optics and Fine Mechanics (AIOFM) (Wang et al., 2015, 2017a).
348 Its telescope is pointed to the north and records at five elevation angles (5°, 10°,
349 20°, 30° and 90°). Wuxi is a typical urban site affected by heavy $NO_x$ and
350 aerosol pollution. The measurements used here are analyzed in Wang et al. (2017a).
351 Data are available in 2012 for comparison with OMI products.

352 When comparing the three OMI products against MAX-DOAS observations, temporal
353 and spatial inconsistency in sampling is inevitable. The spatial inconsistency, together
354 with the substantial horizontal inhomogeneity in $NO_2$, might be more important than
355 the influence of temporal inconsistency (Wang et al., 2017b). The influence of the
356 horizontal inhomogeneity was suggested to be about 10–30% for MAX-DOAS
357 measurements in Beijing (Lin et al., 2014b; Ma et al., 2013) and 10–15% for less
358 polluted locations like Tai'an, Mangshan and Rudong (Irie et al., 2012). Following
359 previous studies (Lin et al., 2014b; Wang et al., 2015, 2017b), we average
360 MAX-DOAS data within 2 h of the OMI overpass time, and we select OMI pixels
361 within 25 km of a MAX-DOAS site whose viewing zenith angle is below 30°. To
362 exclude local pollution events near the MAX-DOAS site (such as the abrupt increase
363 of $NO_2$ caused by the pass of consequent vehicles during a very short period), the
364 standard deviation of MAX-DOAS data within 2 h should not exceed 20% of their



365 mean value (Lin et al., 2014b). We elect not to spatially average the OMI pixels
366 because they can, to some degree, reflect the spatial variability in $NO_2$ and aerosols to
367 some degree.

368 We further exclude MAX-DOAS data in cloudy conditions, as clouds can cause large
369 uncertainties in MAX-DOAS and OMI data. To find the actual cloudy days, we use
370 MODIS/Aqua cloud fraction data, MODIS/Aqua Level-3 corrected reflectance (true
371 color) data at the 1□ x 1□ resolution, and current weather data observed from the
372 nearest ground meteorological station (indicated by the black triangles in Fig. 2b).
373 Since there is only one meteorological station available near the Beijing area, it is
374 used for both IAP and Xianghe MAX-DOAS sites. We first use MODIS/Aqua
375 corrected reflectance (true color) to distinguish clouds from haze. For cloudy days
376 determined by the reflectance checking, we examine both the MODIS/Aqua cloud
377 fraction data and the meteorological station cloud records, considering that
378 MODIS/Aqua cloud fraction data may be missing or have a too coarse horizontal
379 resolution to accurately interpret the cloud conditions at the MAX-DOAS site. We
380 exclude MAX-DOAS $NO_2$ data if the MODIS/Aqua cloud fraction is larger than 60%
381 and the meteorological station reports a “BROKEN” (cloud fraction ranges from 5/8
382 to 7/8) or “OVERCAST” (full cloud cover) sky. For the three MAX-DOAS sites
383 together, this leads to 49 days with valid data out of 64 days with pre-screening data.

384 We note here that using cloud fraction data from MODIS/Aqua or MAX-DOAS (for
385 Xianghe only, see Gielen et al., 2014) alone to screen cloudy scenes may not be
386 appropriate on heavy-haze days. For example, on 8$^{th}$ January, 2012, MODIS/Aqua
387 cloud fraction is about 70–80% over the North China Plain and MAX-DOAS at
388 Xianghe suggests the presence of “thick clouds”. However, both the meteorological
389 station and MODIS/Aqua corrected reflectance (true color) product suggest that the
390 North China Plain was covered by a thick layer of haze. Consequently, this day was
391 excluded from the analysis.

Atmos. Meas. Tech. Discuss., https://doi.org/10.5194/amt-2018-34
Manuscript under review for journal Atmos. Meas. Tech.
Discussion started: 7 March 2018




## 3. Monthly climatology of aerosol extinction profiles from CALIOP and GEOS-Chem

### *3.1 CALIOP monthly climatology*

The ALH is a good indicator to what extent aerosols are mixed vertically. Figure 3a shows the spatial distribution of our CALIOP ALH climatology in each season. At most places, the ALH reaches a maximum in spring or summer and a minimum in fall or winter. The lowest ALH in fall and winter can be attributed to heavy near-surface pollution and weak vertical transport. The high values in summer are related to strong convective activities. Over the north, the high values in spring are partly associated with Asian dust events, due to high surface winds and dry soil in this season (Huang et al., 2010; Proestakis et al., 2017; Wang et al., 2010), which also affects the oceanic regions via atmospheric transport. The springtime high ALH over the south may be related to the transport of carbonaceous aerosols from Southeast Asian biomass burning (Jethva et al., 2016). Averaged over the domain, the seasonal mean ALHs are 1.48 km, 1.43 km, 1.27km, 1.18 km in spring, summer, fall and winter.

Figure 4a,b further shows the climatological monthly variations of ALH averaged over Northern East China (the anthropogenic source region shown in orange in Fig. 2a) and Northwest China (the dust source region shown in yellow in Fig. 2a). The two regions exhibit distinctive temporal variations. Over Northern East China, the ALH reaches a maximum in April (~1.53 km) and a minimum in December (~1.14 km). Over Northwest China, the ALH peaks in August (~1.59km) because of strongest convection (Zhu et al., 2013), although the springtime ALH is also high.

Figure 5a shows the climatological seasonal regional average vertical profiles of aerosol extinction over Northern East China. Here, the aerosol extinction increases from the ground level to a peak at about 300–600 m (season dependent), above which it decreases gradually. The height of peak extinction is lowest in winter, consistent



418 with a stagnant atmosphere, thin mixing layer, and increased emissions (from
419 residential and industrial sectors). The large error bars (horizontal lines in different
420 layers, standing for 1 standard deviation) indicate strong spatiotemporal variability of
421 aerosol extinction.

422 Over Northwest China (Fig. 6a), the column total aerosol extinction is much smaller
423 than that over Northern East China (Fig. 5a), due to lower anthropogenic sources and
424 dominant natural dust emissions. Vertically, the decline of extinction from the
425 peak-extinction height to 2 km is also much more gradual than the decline over
426 Northern East China, indicating stronger lifting of surface emitted aerosols. In winter,
427 the column total aerosol extinction is close to the high value in dusty spring, whereas
428 the vertical gradient of extinction is strongest among the seasons. This reflects the
429 high anthropogenic emissions in parts of Northwest China, which have been rapidly
430 increasing in the 2000s due to relatively weak emission control supplemented by
431 growing activities of relocation of polluted industries from the eastern coastal regions
432 (Cui et al., 2016; Zhao et al., 2015).

433 Overall, the spatial and seasonal variations of CALIOP aerosol vertical profiles are
434 consistent with changes in meteorological conditions, anthropogenic sources, and
435 natural emissions. The data will be used to evaluate and adjust GEOS-Chem
436 simulation results in Sect. 3.3.

437 *3.2 Comparison to NASA CALIOP monthly climatology*

438 We compare our gridded climatological profiles to NASA CALIOP Version 3
439 Level-3 all-sky monthly profiles at 532 nm (Winker et al., 2013). The NASA Level-3
440 data has a horizontal resolution of 2 ° lat. × 5 ° lon. and a vertical resolution of 60
441 m (from -0.5 to 12 km above sea level). We combine NASA monthly data over 2007–
442 2015 to construct a monthly climatology for comparison with our own compilation.
443 We only choose aerosol extinction data in the troposphere with error less than 0.15



(the valid range given in the CALIOP dataset). If the number of valid monthly profiles in a grid cell is less than five (i.e., for the same month in five out of the nine years), then we exclude data in that grid cell; see the dark gray grid cells in Fig. 3c.

Several methodological differences exist between generating our and NASA CALIOP datasets. First, the two datasets have different horizontal resolutions. Also, we sample all valid CALIOP pixels within 1.5□ of a grid cell center, whereas the NASA dataset samples all valid pixels within a grid cell. Besides, our CALIOP dataset involves several steps of horizontal interpolation, for purposes of subsequent cloud and $NO_2$ retrievals, which is not done in the NASA dataset. In addition, we match CALIOP data vertically to the GEOS-Chem vertical resolution, whereas the NASA dataset maintains the original resolution.

Figure 3c shows the spatial distribution of ALH in all seasons based on NASA CALIOP Level-3 all-sky monthly climatology. The horizontal resolution of NASA data is much coarser than ours; and NASA data are largely missing over the southwest with complex terrains. We choose to focus on the comparison over East China (the black box in Fig. 2a). Over East China, the two climatology datasets generally exhibit similar spatial patterns of ALH in all seasons (Fig. 3a, c). The NASA dataset suggests higher ALHs than ours over Eastern China, especially in summer, due mainly to differences in the sampling and regridding processes. Figure 4c further compares the monthly variation of ALH between our (black line with error bars) and NASA (blue filled triangles) datasets averaged over East China. The two datasets are consistent in almost all months, indicating that their regional differences are largely smoothed out by spatial averaging.

### *3.3 Evaluation of GEOS-Chem aerosol extinction profiles*

Figure 3b show the spatial distribution of seasonal ALHs simulated by GEOS-Chem. The model captures the spatial and seasonal variations of CALIOP ALH (Fig. 3a) to



some degree, with an underestimate by about 0.3 km on average. The spatial correlation between CALIOP (Fig. 3a) and GEOS-Chem (Fig. 3b) ALH is 0.37 in spring, 0.57 in summer, 0.40 in fall, and 0.44 in winter. The spatiotemporal consistency and underestimate is also clear from the regional mean monthly ALH data in Fig. 4 – the temporal correlation between GEOS-Chem and CALIOP ALH is 0.90 in Northern East China and 0.97 in Northwest China.

Figures 5a and 6a show the GEOS-Chem simulated 2007–2015 monthly climatological vertical profiles of aerosol extinction coefficient over Northern East China and Northwest China, respectively. Over Northern East China (Fig. 5a), the model (red line) captures the vertical distribution of CALIOP extinction (black line) below the height of 1 km, despite a slight underestimate in the magnitude of extinction and an overestimate in the peak-extinction height. From 1 to 5 km above the ground, the model substantially overestimates the rate of decline in extinction coefficient with increasing altitude. Across the seasons, GEOS-Chem underestimates the magnitude of aerosol extinction by up to 37% (depending on the height). Over Northwest China (Fig. 6a), GEOS-Chem has an underestimate in all seasons, with the largest bias by about 80% in winter likely due to underestimated water-soluble aerosols and dust emissions (Li et al., 2016; Wang et al., 2008a).

Since the POMINO v1.1 algorithm uses MODIS AOD to adjust model AOD, it only uses the CALIOP aerosol extinction profile shape to adjust the modeled shape (Eqs. 2 and 3). Figures 5b and 6b show the vertical shapes of aerosol extinction, averaged across all profiles in each season over Northern East China and Northwest China, respectively. Over Northern East China (Fig. 5b), GEOS-Chem underestimates the CALIOP values above 1 km by 52–71%. This underestimate leads to a lower ALH, consistent with the finding by van Donkelaar et al. (2013) and Lin et al. (2014b). Over Northwest China (Fig. 6b), the model also underestimates the CALIOP values above



1 km by 50–62%. These results imply the importance of correcting the modeled aerosol vertical shape prior to cloud and $NO_2$ retrievals.

## 4. Effects of aerosol vertical profile improvement on cloud retrieval in 2012

Figure 7a, b shows the monthly average ALH and cloud top height (CTH, corresponding to cloud pressure, CP) over Northern East China and Northwest China in 2012. In order to discuss the CTH, only cloudy days are analyzed here, by excluding days with zero cloud fraction (CF = 0, clear-sky cases) in POMINO. Although "clear sky" is used sometimes in the literature to represent low cloud coverage (e.g., CF < 0.2 or CRF < 0.5, Boersma et al., 2011; Chimot et al., 2016), here it strictly means CF = 0 while "cloudy sky" means CF > 0. About 62.7% of days contain non-zero fractions of clouds over Northern East China, and the number is 59.1% for Northwest China. The CF changes from POMINO to POMINO v1.1 (i.e., after aerosol vertical profile adjustment) are negligible (within $\pm$0.5%, not shown) due to the same values of AOD and SSA used in both products. This is because overall CF is mostly driven by the continuum reflectance at 475 nm, which is independent of aerosol profile but CTH is driven by the $O_2$-$O_2$ SCD, which is itself impacted by ALH.

Figure 7a, b shows that over the two regions, the CTH varies notably from one month to another, whereas the ALH is much more stable across the months. Over Northern East China, the ALH increases by 0.52 km from POMINO (orange dashed line) to POMINO v1.1 (orange solid line) due to the CALIOP-based monthly climatological adjustment. The increase in ALH means a stronger "shielding" effect of aerosols on the $O_2$-$O_2$ absorbing dimer which, in turn, results in a reduced CTH by 0.69 km on average. For POMINO over Northern East China (Fig. 7a), the retrieved clouds usually extend above the aerosol layer, i.e., the CTH (grey dashed line) is much larger than the ALH (orange dashed line). Using the CALIOP climatology in POMINO v1.1 results in the ALH higher than the CTH in fall and winter. The more elevated ALH is



consistent with the finding of Jethva et al. (2016) that a significant amount of absorbing aerosols reside above clouds over Northern East China based on 11-year (2004–2015) OMI near-UV observations.

The CTH in Northwest China is much lower than in Northern East China (Fig. 7a versus 7b). This is because the dominant type of actual clouds is (optically thin) cirrus over western China (Wang et al., 2014), which is interpreted by the $O_2$-$O_2$ cloud retrieval algorithm as reduced CTH (with cloud base from the ground). The reduction in CTH from POMINO to POMINO v1.1 over Northwest China is also smaller than the reduction over Northern East China, albeit with a similar enhancement in ALH, due to lower aerosol loadings (Fig. 7c versus 7d).

Figure 8g, h presents the relative change in CP from POMINO to POMINO v1.1 as a function of AOD (binned at an interval of 0.1) and changes in ALH from POMINO to POMINO v1.1 ($\Delta$ALH, binned every 0.2 km) across all pixels in 2012 over Northern East China. Results are separated for low cloud fraction (CF < 0.05 in POMINO, Fig. 8g) and modest cloud fraction (0.2 < CF < 0.3, Fig. 8h). The median of the CP changes for pixels within each AOD and $\Delta$ALH bin is shown. Figure 8e,f presents the corresponding numbers of occurrence under the two cloud conditions.

Figure 8 shows that over Northern East China, the increase in ALH is typically within 0.6 km for the case of CF < 0.05 (Fig. 8e), and the corresponding increase in CP is within 6% (Fig. 8g). In this case, the average CTH (2.95 km in POMINO versus 1.58 km in POMINO v1.1) becomes much lower than the average ALH (1.06 km in POMINO versus 1.98 km in POMINO v1.1). For the case with CF between 0.2 and 0.3, the increase in ALH is within 1.2 km for most scenes (Fig. 8f), which leads to a CP change of 2% (Fig. 8h), much smaller than the CP change for CF < 0.05 (Fig. 8g). This is partly because the larger the CF is, the smaller a change in CF is required to compensate for the $\Delta$ALH in the $O_2$-$O_2$ cloud retrieval algorithm. Furthermore, with 0.2 < CF < 0.3, the mean value of CTH is much higher than ALH in both POMINO



(2.76 km for CTH versus 1.13km for ALH) and POMINO v1.1 (2.60km for CTH versus 2.09 km for ALH), thus a large portion of clouds are above aerosols so that the change in CP is less sensitive to ΔALH. We find that the summertime data contribute the highest portion (36.5%) to the occurrences for $0.2 < CF < 0.3$.

For Northwest China (not shown), the dependence of CP changes to AOD and ΔALH is similar to that for Northern East China. In particular, the CP change is within 10% on average for the case of $CF < 0.05$ and 1.5% for the case of $0.2 < CF < 0.3$.

## 5. Effects of aerosol vertical profile improvement on $NO_2$ retrieval in 2012

Figure 8a presents the percentage changes in clear-sky $NO_2$ VCD from POMINO to POMINO v1.1 as a function of binned AOD and ΔALH over Northern East China. Here, clear-sky pixels are chosen based on CF = 0 in POMINO. In any AOD bin, an increase in ΔALH leads to an enhancement in $NO_2$. And for any ΔALH, the change in VCD is greater (smaller) when AOD becomes larger (smaller), which indicates that the $NO_2$ retrieval is more sensitive to ALH in high aerosol loading cases. Clearly, the change in $NO_2$ is not a linear function of AOD and ΔALH.

For cloudy scenes (Fig. 8b, c, cloud data are based on POMINO), the change in $NO_2$ VCD is less sensitive to AOD and ΔALH. This is because the existence of clouds limits the optical effect of aerosols on tropospheric $NO_2$. Figure 7a presents the nitrogen layer height (NLH, defined as the average height of model simulated $NO_2$ weighted by its volume mixing ratio in each layer) in comparison to the ALH and CLH over Northern East China. The figure shows that the POMINO v1.1 CTH is higher than the NLH in all months and higher than the ALH in warm months, which means a “shielding” effect on both $NO_2$ and aerosols.

Over Northwest China (not shown), the changes in clear-sky $NO_2$ VCD are within 9% for most cases, which are much smaller than over Eastern China (within 18%). This is



because the NLH is much higher than the CLH and ALH (Fig. 7b) in absence of surface anthropogenic emissions.

We convert the valid pixels into monthly mean Level-3 values datasets on a 0.25° long. × 0.25° lat. grid. Figure 9a, b compares the seasonal spatial variations of $NO_2$ VCD in POMINO v1.1 and POMINO in 2012. In both products, $NO_2$ peaks in winter due to the longest lifetime and highest anthropogenic emissions (Lin, 2012). $NO_2$ also reaches a maximum over Northern East China as a result of substantial anthropogenic sources. From POMINO to POMINO v1.1, the $NO_2$ VCD increases by 3.4% (-67.5–41.7%) in spring for the domain average (range), 3.0% (-59.5–34.4%) in summer, 4.6% (-15.3–39.6%) in fall and 5.3% (-68.4–49.3%) in winter. The $NO_2$ change is highly dependent on the location and season. The increase over Northern East China is largest in winter, wherein the positive ΔALH mean elevated aerosol layers that better "shield" the $NO_2$ absorption.

## 6. Evaluating satellite products using MAX-DOAS data

We use MAX-DOAS data, after cloud screening (Sect. 2.4), to evaluate DOMNO v2, POMINO and POMINO v1.1. The scatterplots in Fig. 10a-c compare the $NO_2$ VCDs from 162 OMI pixels on 49 days with their MAX-DOAS counterparts. Different colors differentiate the seasons. The high values of $NO_2$ VCD (> 30 × $10^{15}$ molec. $cm^{-2}$) occur mainly in fall (blue) and winter (black). POMINO v1.1 and POMINO capture the day-to-day variability of MAX-DOAS data, i.e., $R^2$ = 0.804 and 0.799, respectively. The normalized mean bias (NMB) of POMINO v1.1 relative to MAX-DOAS data (-3.4%) is smaller than the NMB of POMINO (-9.6%). Also, the reduced major axis (RMA) regression shows that the slope for POMINO v1.1 (0.95) is closer to unity than the slope for POMINO (0.78). When all OMI pixels in a day are averaged (Fig. 11d, e), the correlation across the total of 49 days further increase for both POMINO v1.1 ($R^2$ = 0.89) and POMINO ($R^2$ = 0.86), whereas POMINO v1.1 still has a lower NMB (-3.7%) and better slope (0.96) than POMINO (-10.4% and



602 0.82, respectively). These results suggest that correcting aerosol vertical profiles, at
603 least on a climatology basis, already leads to a significant improved $NO_2$ retrieval
604 from OMI.

605 Figure 10c, f shows that DOMINO v2 is correlated with MAX-DOAS ($R^2$ = 0.68 in
606 Fig. 10c and 0.75 in Fig. 10f) but not as well as POMINO and POMINO v1.1. The
607 discrepancy between DOMINO v2 and MAX-DOAS is particularly large for very
608 high $NO_2$ values (> 70 × $10^{15}$ molec. $cm^{-2}$). These results are consistent with the
609 finding of Lin et al. (2014b, 2015) that explicitly including aerosol optical effects
610 improves the $NO_2$ retrieval.

611 Table 3 further shows the comparison statistics for 27 haze days. The haze days are
612 determined when both the ground meteorological station data and MODIS/Aqua
613 corrected reflectance (true color) data indicate a haze day. The table also lists AOD,
614 SSA, CF and MAX-DOAS $NO_2$ VCD, as averaged over all haze days. A large
615 amount of absorbing aerosols occurs on these haze days (AOD = 1.13, SSA = 0.90).
616 The average MAX-DOAS $NO_2$ VCD reaches 51.92 × $10^{15}$ molec. $cm^{-2}$. Among the
617 three satellite products, POMINO v1.1 has the highest $R^2$ (0.76) and the lowest bias
618 (4.4%) with respect to MAX-DOAS, whereas DOMINO v2 reproduces the variability
619 to a limited extent ($R^2$ = 0.38). This is consistent with the previous finding that the
620 accuracy of DOMINO v2 is reduced for polluted, aerosol-loaded scenes (Boersma et
621 al., 2011; Chimot et al., 2016; Kanaya et al., 2014; Lin et al., 2014b).

622 Table 4 shows the comparison statistics for 36 cloud-free days (CF = 0 in POMINO).
623 Here, the three OMI products do not show large differences in $R^2$ (0.53–0.56) and
624 NMB (20.8–29.4%) with respect to MAX-DOAS. However, the $R^2$ values for
625 POMINO and POMINO v1.1 are much smaller than the $R^2$ values in haze days,
626 whereas the opposite change is true for DOMINO v2. Thus, for this limited set of
627 data, the change from DOMINO v2 to POMINO and POMINO v1.1 mainly reflect



628 the improved aerosol treatment in hazy scenes. Further research may use additional
629 MAX-DOAS datasets to evaluate the satellite products more systematically.

630 **7. Conclusions**

631 This paper improves upon our previous POMINO algorithm (Lin et al., 2015) to
632 retrieve the tropospheric $NO_2$ VCDs from OMI, by compiling a 9-year (2007–2015)
633 CALIOP monthly climatology of aerosol vertical extinction profiles to adjust
634 GEOS-Chem aerosol profiles used in the $NO_2$ retrieval process. The improved
635 product is referred to as POMINO v1.1. Compared to monthly climatological
636 CALIOP data over China, GEOS-Chem simulations tend to underestimate the aerosol
637 extinction above 1 km, as characterized by an underestimate in ALH by 300–600 m
638 (seasonal and location dependent). Such a bias is corrected in POMINO v1.1 by
639 dividing, for any month and grid cell, the CALIOP monthly climatological profile by
640 the model climatological profile to obtain a scaling profile and then applying the
641 scaling profile to model data in all days of that month in all years.

642 The aerosol extinction profile correction leads to an insignificant change in CF from
643 POMINO to POMINO v1.1, since the AOD and surface reflectance are unchanged. In
644 contrast, the correction results in a notably increase in CP (i.e., a decrease in CTH),
645 due to lifting of aerosol layers. The CP changes are generally within 6% for scenes
646 with low cloud fraction (CF < 0.05 in POMINO), and within 2% for scenes with
647 modest cloud fraction (0.2 < CF < 0.3 in POMINO).

648 The $NO_2$ VCDs increase from POMINO to POMINO v1.1 in most cases due to lifting
649 of aerosol layers that enhances the "shielding" of $NO_2$ absorption. The $NO_2$ VCD
650 increases by 3.4% (-67.5–41.7%) in spring for the domain average (range), 3.0%
651 (-59.5–34.4%) in summer, 4.6% (-15.3–39.6%) in fall and 5.3% (-68.4–49.3%) in
652 winter. The $NO_2$ changes highly season and location dependent, and are most
653 significant for wintertime Northern East China.



Further comparisons with independent MAX-DOAS $NO_2$ VCD data for 162 OMI pixels in 49 days show good performance of both POMINO v1.1 and POMINO in capturing the day-to-day variation of $NO_2$ ($R^2$=0.80, n=162), compared to DOMINO v2 ($R^2$=0.67). The NMB is smaller in POMINO v1.1 (-3.4%) than in POMINO (-9.6%), with a slightly better slope (0.80 versus 0.78). On hazy days with high aerosol loadings (AOD = 1.13 on average), POMINO v1.1 has the highest $R^2$ (0.76) and the lowest bias (4.4%) whereas DOMINO has difficulty in reproducing the day-to-day variability in MAX-DOAS $NO_2$ measurements ($R^2$ = 0.38). The three products show small differences in $R^2$ and NMB on clear-sky days (CF = 0 in POMINO, AOD = 0.60 on average). Thus the explicit aerosol treatment (in POMINO and POMINO v1.1) and the aerosol vertical profile correction (in POMINO v1.1) improves the $NO_2$ retrieval especially in hazy cases.

Our POMINO v1.1 algorithm is being applied to the recently launched TropOMI instrument that provides $NO_2$ information at a much higher spatial resolution (3.5 x 7 $km^2$). A modified algorithm can also be used to retrieve sulfur dioxide, formaldehyde and other trace gases from TropOMI, for which purposes our algorithm will be available to the community on a collaborative basis. Future research can correct the SSA and $NO_2$ vertical profile to further improve the retrieval algorithm, and can use more comprehensive independent data to evaluate the resulting satellite products.

## Acknowledgements

This research is supported by the National Natural Science Foundation of China (41775115), the 973 program (2014CB441303), the Chinese Scholarship Council, and the EU FP7 QA4ECV project (grant no. 607405).

## References

Acarreta, J. R., De Haan, J. F. and Stammes, P.: Cloud pressure retrieval using the $O_2$ -$O_2$ absorption band at 477 nm, J. Geophys. Res., 109(D5), D05204, doi:10.1029/2003JD003915, 2004.



Amiridis, V., Marinou, E., Tsekeri, A., Wandinger, U., Schwarz, A., Giannakaki, E., Mamouri, R., Kokkalis, P., Binietoglou, I., Solomos, S., Herekakis, T., Kazadzis, S., Gerasopoulos, E., Proestakis, E., Kottas, M., Balis, D., Papayannis, A., Kontoes, C., Kourtidis, K., Papagiannopoulos, N., Mona, L., Pappalardo, G., Le Rille, O. and Ansmann, A.: LIVAS: a 3-D multi-wavelength aerosol/cloud database based on CALIPSO and EARLINET, Atmos. Chem. Phys., 15(13), 7127–7153, doi:10.5194/acp-15-7127-2015, 2015.

Belmonte Rivas, M., Veefkind, P., Boersma, F., Levelt, P., Eskes, H. and Gille, J.: Intercomparison of daytime stratospheric NO2 satellite retrievals and model simulations, Atmos. Meas. Tech., 7(7), 2203–2225, doi:10.5194/amt-7-2203-2014, 2014.

Boersma, K. F., Eskes, H. J. and Brinksma, E. J.: Error analysis for tropospheric $NO_2$ retrieval from space, J. Geophys. Res. Atmos., 109(D4), n/a-n/a, doi:10.1029/2003JD003962, 2004.

Boersma, K. F., Eskes, H. J., Veefkind, J. P., Brinksma, E. J., van der A, R. J., Sneep, M., van den Oord, G. H. J., Levelt, P. F., Stammes, P., Gleason, J. F. and Bucsela, E. J.: Near-real time retrieval of tropospheric NO2 from OMI, Atmos. Chem. Phys., 7(8), 2103–2118, doi:10.5194/acp-7-2103-2007, 2007.

Boersma, K. F., Eskes, H. J., Dirksen, R. J., van der A, R. J., Veefkind, J. P., Stammes, P., Huijnen, V., Kleipool, Q. L., Sneep, M., Claas, J., Leitão, J., Richter, A., Zhou, Y. and Brunner, D.: An improved tropospheric NO2 column retrieval algorithm for the Ozone Monitoring Instrument, Atmos. Meas. Tech., 4(9), 1905–1928, doi:10.5194/amt-4-1905-2011, 2011.

Bucsela, E. J., Celarier, E. A., Wenig, M. O., Gleason, J. F., Veefkind, J. P., Boersma, K. F. and Brinksma, E. J.: Algorithm for NO2 vertical column retrieval from the ozone monitoring instrument, IEEE Trans. Geosci. Remote Sens., 44(5), 1245–1258, doi:10.1109/TGRS.2005.863715, 2006.

Bucsela, E. J., Krotkov, N. A., Celarier, E. A., Lamsal, L. N., Swartz, W. H., Bhartia, P. K., Boersma, K. F., Veefkind, J. P., Gleason, J. F. and Pickering, K. E.: A new stratospheric and tropospheric NO2 retrieval algorithm for nadir-viewing satellite instruments: applications to OMI, Atmos. Meas. Tech., 6(10), 2607–2626, doi:10.5194/amt-6-2607-2013, 2013.

Castellanos, P., Boersma, K. F. and van der Werf, G. R.: Satellite observations indicate substantial spatiotemporal variability in biomass burning NOx emission factors for South America, Atmos. Chem. Phys., 14(8), 3929–3943, doi:10.5194/acp-14-3929-2014, 2014.



717 Castellanos, P., Boersma, K. F., Torres, O. and de Haan, J. F.: OMI tropospheric NO2
718 air mass factors over South America: effects of biomass burning aerosols, Atmos.
719 Meas. Tech., 8(9), 3831–3849, doi:10.5194/amt-8-3831-2015, 2015.

720 Chazette, P., Raut, J.-C., Dulac, F., Berthier, S., Kim, S.-W., Royer, P., Sanak, J.,
721 Loaëc, S. and Grigaut-Desbrosses, H.: Simultaneous observations of lower
722 tropospheric continental aerosols with a ground-based, an airborne, and the spaceborne
723 CALIOP lidar system, J. Geophys. Res., 115(D4), D00H31,
724 doi:10.1029/2009JD012341, 2010.

725 Chimot, J., Vlemmix, T., Veefkind, J. P., de Haan, J. F. and Levelt, P. F.: Impact of
726 aerosols on the OMI tropospheric NO2 retrievals over industrialized regions: how
727 accurate is the aerosol correction of cloud-free scenes via a simple cloud model?,
728 Atmos. Meas. Tech., 9(2), 359–382, doi:10.5194/amt-9-359-2016, 2016.

729 Clémer, K., Van Roozendael, M., Fayt, C., Hendrick, F., Hermans, C., Pinardi, G.,
730 Spurr, R., Wang, P. and De Mazière, M.: Multiple wavelength retrieval of tropospheric
731 aerosol optical properties from MAXDOAS measurements in Beijing, Atmos. Meas.
732 Tech., 3(4), 863–878, doi:10.5194/amt-3-863-2010, 2010.

733 Cui, Y., Lin, J., Song, C., Liu, M., Yan, Y., Xu, Y. and Huang, B.: Rapid growth in
734 nitrogen dioxide pollution over Western China, 2005–2013, Atmos. Chem. Phys.,
735 16(10), 6207–6221, doi:10.5194/acp-16-6207-2016, 2016.

736 Dirksen, R. J., Boersma, K. F., Eskes, H. J., Ionov, D. V., Bucsela, E. J., Levelt, P. F.
737 and Kelder, H. M.: Evaluation of stratospheric $NO_2$ retrieved from the Ozone
738 Monitoring Instrument: Intercomparison, diurnal cycle, and trending, J. Geophys. Res.,
739 116(D8), D08305, doi:10.1029/2010JD014943, 2011.

740 van Geffen, J. H. G. M., Boersma, K. F., Van Roozendael, M., Hendrick, F., Mahieu,
741 E., De Smedt, I., Sneep, M. and Veefkind, J. P.: Improved spectral fitting of nitrogen
742 dioxide from OMI in the 405–465 nm window, Atmos. Meas. Tech., 8(4), 1685–1699,
743 doi:10.5194/amt-8-1685-2015, 2015.

744 Gielen, C., Van Roozendael, M., Hendrick, F., Pinardi, G., Vlemmix, T., De Bock, V.,
745 De Backer, H., Fayt, C., Hermans, C., Gillotay, D. and Wang, P.: A simple and versatile
746 cloud-screening method for MAX-DOAS retrievals, Atmos. Meas. Tech., 7(10), 3509–
747 3527, doi:10.5194/amt-7-3509-2014, 2014.

748 Huang, Z., Huang, J., Bi, J., Wang, G., Wang, W., Fu, Q., Li, Z., Tsay, S.-C. and Shi, J.:
749 Dust aerosol vertical structure measurements using three MPL lidars during 2008
750 China-U.S. joint dust field experiment, J. Geophys. Res. Atmos., 115(D7),
751 doi:10.1029/2009JD013273, 2010.

752 Irie, H., Boersma, K. F., Kanaya, Y., Takashima, H., Pan, X. and Wang, Z. F.:
753 Quantitative bias estimates for tropospheric NO2 columns retrieved from



754 SCIAMACHY, OMI, and GOME-2 using a common standard for East Asia, Atmos.
755 Meas. Tech., 5(10), 2403–2411, doi:10.5194/amt-5-2403-2012, 2012.

756 Johnson, M. S., Meskhidze, N. and Praju Kiliyanpilakkil, V.: A global comparison of
757 GEOS-Chem-predicted and remotely-sensed mineral dust aerosol optical depth and
758 extinction profiles, J. Adv. Model. Earth Syst., 4(3), M07001,
759 doi:10.1029/2011MS000109, 2012.

760 Kacenelenbogen, M., Redemann, J., Vaughan, M. A., Omar, A. H., Russell, P. B.,
761 Burton, S., Rogers, R. R., Ferrare, R. A. and Hostetler, C. A.: An evaluation of
762 CALIOP/CALIPSO's aerosol-above-cloud detection and retrieval capability over
763 North America, J. Geophys. Res. Atmos., 119(1), 230–244,
764 doi:10.1002/2013JD020178, 2014.

765 Kanaya, Y., Irie, H., Takashima, H., Iwabuchi, H., Akimoto, H., Sudo, K., Gu, M.,
766 Chong, J., Kim, Y. J., Lee, H., Li, A., Si, F., Xu, J., Xie, P.-H., Liu, W.-Q., Dzhola, A.,
767 Postylyakov, O., Ivanov, V., Grechko, E., Terpugova, S. and Panchenko, M.:
768 Long-term MAX-DOAS network observations of NO2 in Russia and Asia (MADRAS)
769 during the period 2007-2012: instrumentation, elucidation of climatology, and
770 comparisons with OMI satellite observations and global model simulations, Atmos.
771 Chem. Phys., 14(15), 7909–7927, doi:10.5194/acp-14-7909-2014, 2014.

772 Kim, S.-W., Heckel, A., Frost, G. J., Richter, A., Gleason, J., Burrows, J. P., McKeen,
773 S., Hsie, E.-Y., Granier, C. and Trainer, M.: $NO_2$ columns in the western United States
774 observed from space and simulated by a regional chemistry model and their
775 implications for $NO_x$ emissions, J. Geophys. Res., 114(D11), D11301,
776 doi:10.1029/2008JD011343, 2009.

777 Koffi, B., Schulz, M., Bréon, F.-M., Griesfeller, J., Winker, D., Balkanski, Y., Bauer,
778 S., Berntsen, T., Chin, M., Collins, W. D., Dentener, F., Diehl, T., Easter, R., Ghan, S.,
779 Ginoux, P., Gong, S., Horowitz, L. W., Iversen, T., Kirkevåg, A., Koch, D., Krol, M.,
780 Myhre, G., Stier, P. and Takemura, T.: Application of the CALIOP layer product to
781 evaluate the vertical distribution of aerosols estimated by global models: AeroCom
782 phase I results, J. Geophys. Res. Atmos., 117(D10), n/a-n/a,
783 doi:10.1029/2011JD016858, 2012.

784 Leitão, J., Richter, A., Vrekoussis, M., Kokhanovsky, A., Zhang, Q. J., Beekmann, M.
785 and Burrows, J. P.: On the improvement of NO2 satellite retrievals – aerosol impact on
786 the airmass factors, Atmos. Meas. Tech., 3(2), 475–493, doi:10.5194/amt-3-475-2010,
787 2010.

788 Lerot, C., Stavrakou, T., De Smedt, I., Müller, J.-F. and Van Roozendael, M.: Glyoxal
789 vertical columns from GOME-2 backscattered light measurements and comparisons
790 with a global model, Atmos. Chem. Phys., 10(24), 12059–12072,
791 doi:10.5194/acp-10-12059-2010, 2010.



792 Li, S., Yu, C., Chen, L., Tao, J., Letu, H., Ge, W., Si, Y. and Liu, Y.: Inter-comparison
793 of model-simulated and satellite-retrieved componential aerosol optical depths in
794 China, Atmos. Environ., 141, 320–332,
795 doi:https://doi.org/10.1016/j.atmosenv.2016.06.075, 2016.

796 Lin, J., Pan, D., Davis, S. J., Zhang, Q., He, K., Wang, C., Streets, D. G., Wuebbles, D.
797 J. and Guan, D.: China's international trade and air pollution in the United States, Proc.
798 Natl. Acad. Sci., 111(5), 1736–1741, doi:10.1073/pnas.1312860111, 2014a.

799 Lin, J.-T.: Satellite constraint for emissions of nitrogen oxides from anthropogenic,
800 lightning and soil sources over East China on a high-resolution grid, Atmos. Chem.
801 Phys., 12(6), 2881–2898, doi:10.5194/acp-12-2881-2012, 2012.

802 Lin, J.-T., McElroy, M. B. and Boersma, K. F.: Constraint of anthropogenic NOx
803 emissions in China from different sectors: a new methodology using multiple satellite
804 retrievals, Atmos. Chem. Phys., 10(1), 63–78, doi:10.5194/acp-10-63-2010, 2010.

805 Lin, J.-T., Martin, R. V., Boersma, K. F., Sneep, M., Stammes, P., Spurr, R., Wang, P.,
806 Van Roozendael, M., Clémer, K. and Irie, H.: Retrieving tropospheric nitrogen dioxide
807 from the Ozone Monitoring Instrument: effects of aerosols, surface reflectance
808 anisotropy, and vertical profile of nitrogen dioxide, Atmos. Chem. Phys., 14(3), 1441–
809 1461, doi:10.5194/acp-14-1441-2014, 2014b.

810 Lin, J.-T., Liu, M.-Y., Xin, J.-Y., Boersma, K. F., Spurr, R., Martin, R. and Zhang, Q.:
811 Influence of aerosols and surface reflectance on satellite $NO_2$ retrieval: seasonal and
812 spatial characteristics and implications for $NO_x$ emission constraints, Atmos. Chem.
813 Phys., 15(19), 11217–11241, doi:10.5194/acp-15-11217-2015, 2015.

814 Lorente, A., Folkert Boersma, K., Yu, H., Dörner, S., Hilboll, A., Richter, A., Liu, M.,
815 Lamsal, L. N., Barkley, M., De Smedt, I., Van Roozendael, M., Wang, Y., Wagner, T.,
816 Beirle, S., Lin, J.-T., Krotkov, N., Stammes, P., Wang, P., Eskes, H. J. and Krol, M.:
817 Structural uncertainty in air mass factor calculation for NO2 and HCHO satellite
818 retrievals, Atmos. Meas. Tech., 10(3), 759–782, doi:10.5194/amt-10-759-2017, 2017.

819 Lucht, W., Schaaf, C. B. and Strahler, A. H.: An algorithm for the retrieval of albedo
820 from space using semiempirical BRDF models, IEEE Trans. Geosci. Remote Sens.,
821 38(2), 977–998, doi:10.1109/36.841980, 2000.

822 Ma, J. Z., Beirle, S., Jin, J. L., Shaiganfar, R., Yan, P. and Wagner, T.: Tropospheric
823 NO2 vertical column densities over Beijing: results of the first three years of
824 ground-based MAX-DOAS measurements (2008-2011) and satellite validation,
825 Atmos. Chem. Phys., 13(3), 1547–1567, doi:10.5194/acp-13-1547-2013, 2013.

826 Ma, X. and Yu, F.: Seasonal variability of aerosol vertical profiles over east US and
827 west Europe: GEOS-Chem/APM simulation and comparison with CALIPSO



828 observations, Atmos. Res., 140–141, 28–37,
829 doi:https://doi.org/10.1016/j.atmosres.2014.01.001, 2014.

830 Martin, R. V.: An improved retrieval of tropospheric nitrogen dioxide from GOME, J.
831 Geophys. Res., 107(D20), 4437, doi:10.1029/2001JD001027, 2002.

832 Misra, A., Tripathi, S. N., Kaul, D. S. and Welton, E. J.: Study of MPLNET-Derived
833 Aerosol Climatology over Kanpur, India, and Validation of CALIPSO Level 2 Version
834 3 Backscatter and Extinction Products, J. Atmos. Ocean. Technol., 29(9), 1285–1294,
835 doi:10.1175/JTECH-D-11-00162.1, 2012.

836 Miyazaki, K. and Eskes, H.: Constraints on surface $NO_x$ emissions by assimilating
837 satellite observations of multiple species, Geophys. Res. Lett., 40(17), 4745–4750,
838 doi:10.1002/grl.50894, 2013.

839 Proestakis, E., Amiridis, V., Marinou, E., Georgoulias, A. K., Solomos, S., Kazadzis,
840 S., Chimot, J., Che, H., Alexandri, G., Binietoglou, I., Kourtidis, K. A., de Leeuw, G.
841 and van der A, R. J.: 9-year spatial and temporal evolution of desert dust aerosols over
842 South-East Asia as revealed by CALIOP, Atmos. Chem. Phys. Discuss., 1–35,
843 doi:10.5194/acp-2017-797, 2017.

844 Richter, A., Begoin, M., Hilboll, A. and Burrows, J. P.: An improved NO2 retrieval for
845 the GOME-2 satellite instrument, Atmos. Meas. Tech., 4(6), 1147–1159,
846 doi:10.5194/amt-4-1147-2011, 2011.

847 Sareen, N., Schwier, A. N., Shapiro, E. L., Mitroo, D. and McNeill, V. F.: Secondary
848 organic material formed by methylglyoxal in aqueous aerosol mimics, Atmos. Chem.
849 Phys., 10(3), 997–1016, doi:10.5194/acp-10-997-2010, 2010.

850 Stammes, P., Sneep, M., de Haan, J. F., Veefkind, J. P., Wang, P. and Levelt, P. F.:
851 Effective cloud fractions from the Ozone Monitoring Instrument: Theoretical
852 framework and validation, J. Geophys. Res., 113(D16), D16S38,
853 doi:10.1029/2007JD008820, 2008.

854 Stavrakou, T., Müller, J.-F., Bauwens, M., De Smedt, I., Lerot, C., Van Roozendael,
855 M., Coheur, P.-F., Clerbaux, C., Boersma, K. F., van der A, R. and Song, Y.:
856 Substantial Underestimation of Post-Harvest Burning Emissions in the North China
857 Plain Revealed by Multi-Species Space Observations, Sci. Rep., 6, 32307,
858 doi:10.1038/srep32307, 2016.

859 Veefkind, J. P., de Haan, J. F., Sneep, M. and Levelt, P. F.: Improvements to the OMI
860 O2–O2 operational cloud algorithm and comparisons with ground-based radar–lidar
861 observations, Atmos. Meas. Tech., 9(12), 6035–6049, doi:10.5194/amt-9-6035-2016,
862 2016.

863 Verstraeten, W. W., Neu, J. L., Williams, J. E., Bowman, K. W., Worden, J. R. and
864 Boersma, K. F.: Rapid increases in tropospheric ozone production and export from



China, Nat. Geosci., 8, 690 [online] Available from: http://dx.doi.org/10.1038/ngeo2493, 2015.

Wang, J., Jacob, D. J. and Martin, S. T.: Sensitivity of sulfate direct climate forcing to the hysteresis of particle phase transitions, J. Geophys. Res. Atmos., 113(D11), doi:10.1029/2007JD009368, 2008a.

Wang, M., Gu, J., Yang, R., Zeng, L. and Wang, S.: Comparison of cloud type and frequency over China from surface, FY-2E, and CloudSat observations, vol. 9259, pp. 925913–925914. [online] Available from: http://dx.doi.org/10.1117/12.2069110, 2014.

Wang, P. and Stammes, P.: Evaluation of SCIAMACHY Oxygen A band cloud heights using Cloudnet measurements, Atmos. Meas. Tech., 7(5), 1331–1350, doi:10.5194/amt-7-1331-2014, 2014.

Wang, P., Stammes, P., van der A, R., Pinardi, G. and van Roozendael, M.: FRESCO+: an improved O2 A-band cloud retrieval algorithm for tropospheric trace gas retrievals, Atmos. Chem. Phys., 8(21), 6565–6576, doi:10.5194/acp-8-6565-2008, 2008b.

Wang, X., Huang, J., Zhang, R., Chen, B. and Bi, J.: Surface measurements of aerosol properties over northwest China during ARM China 2008 deployment, J. Geophys. Res. Atmos., 115(D7), n/a-n/a, doi:10.1029/2009JD013467, 2010.

Wang, Y., Penning de Vries, M., Xie, P. H., Beirle, S., Dörner, S., Remmers, J., Li, A. and Wagner, T.: Cloud and aerosol classification for 2.5 years of MAX-DOAS observations in Wuxi (China) and comparison to independent data sets, Atmos. Meas. Tech., 8(12), 5133–5156, doi:10.5194/amt-8-5133-2015, 2015.

Wang, Y., Lampel, J., Xie, P., Beirle, S., Li, A., Wu, D. and Wagner, T.: Ground-based MAX-DOAS observations of tropospheric aerosols, NO2, SO2 and HCHO in Wuxi, China, from 2011 to 2014, Atmos. Chem. Phys., 17(3), 2189–2215, doi:10.5194/acp-17-2189-2017, 2017a.

Wang, Y., Beirle, S., Lampel, J., Koukouli, M., De Smedt, I., Theys, N., Li, A., Wu, D., Xie, P., Liu, C., Van Roozendael, M., Stavrakou, T., Müller, J.-F., and Wagner, T.: Validation of OMI, GOME-2A and GOME-2B tropospheric NO2, SO2 and HCHO products using MAX-DOAS observations from 2011 to 2014 in Wuxi, China: investigation of the effects of priori profiles and aerosols on the satellite products, Atmos. Chem. Phys., 17, 5007-5033, https://doi.org/10.5194/acp-17-5007-2017, 2017b.

Winker, D. M., Pelon, J., Coakley, J. A., Ackerman, S. A., Charlson, R. J., Colarco, P. R., Flamant, P., Fu, Q., Hoff, R. M., Kittaka, C., Kubar, T. L., Le Treut, H., Mccormick, M. P., Mégie, G., Poole, L., Powell, K., Trepte, C., Vaughan, M. A. and Wielicki, B. A.: The CALIPSO Mission, Bull. Am. Meteorol. Soc., 91(9), 1211–1230, doi:10.1175/2010BAMS3009.1, 2010.



902 Winker, D. M., Tackett, J. L., Getzewich, B. J., Liu, Z., Vaughan, M. A. and Rogers, R.
903 R.: The global 3-D distribution of tropospheric aerosols as characterized by CALIOP,
904 Atmos. Chem. Phys., 13(6), 3345–3361, doi:10.5194/acp-13-3345-2013, 2013.

905 Zara, M., Boersma, K. F., De Smedt, I., Richter, A., Peters, E., Van Geffen, J. H. G. M.,
906 Beirle, S., Wagner, T., Van Roozendael, M., Marchenko, S., Lamsal, L. N. and Eskes,
907 H. J.: Improved slant column density retrieval of nitrogen dioxide and formaldehyde
908 for OMI and GOME-2A from QA4ECV: intercomparison, uncertainty
909 characterization, and trends, Atmos. Meas. Tech. Discuss., 1–47,
910 doi:10.5194/amt-2017-453, 2018.

911 Zhang, Q., Streets, D. G., Carmichael, G. R., He, K. B., Huo, H., Kannari, A., Klimont,
912 Z., Park, I. S., Reddy, S., Fu, J. S., Chen, D., Duan, L., Lei, Y., Wang, L. T. and Yao, Z.
913 L.: Asian emissions in 2006 for the NASA INTEX-B mission, Atmos. Chem. Phys.,
914 9(14), 5131–5153, doi:10.5194/acp-9-5131-2009, 2009.

915 Zhao, C. and Wang, Y.: Assimilated inversion of $NO_x$ emissions over east Asia using
916 OMI $NO_2$ column measurements, Geophys. Res. Lett., 36(6), L06805,
917 doi:10.1029/2008GL037123, 2009.

918 Zhao, H. Y., Zhang, Q., Guan, D. B., Davis, S. J., Liu, Z., Huo, H., Lin, J. T., Liu, W. D.
919 and He, K. B.: Assessment of China's virtual air pollution transport embodied in trade
920 by using a consumption-based emission inventory, Atmos. Chem. Phys., 15(10), 5443–
921 5456, doi:10.5194/acp-15-5443-2015, 2015.

922 Zhou, Y., Brunner, D., Spurr, R. J. D., Boersma, K. F., Sneep, M., Popp, C. and
923 Buchmann, B.: Accounting for surface reflectance anisotropy in satellite retrievals of
924 tropospheric NO2, Atmos. Meas. Tech., 3(5), 1185–1203,
925 doi:10.5194/amt-3-1185-2010, 2010.

926 Zhu, W., Xu, C., Qian, X. and Wei, H.: Statistical analysis of the spatial-temporal
927 distribution of aerosol extinction retrieved by micro-pulse lidar in Kashgar, China, Opt.
928 Express, 21(3), 2531–2537, doi:10.1364/OE.21.002531, 2013.

929 Hendrick, F., Muller, J. F., Clemer, K., Wang, P., De Maziere, M., Fayt, C., Gielen, C.,
930 Hermans, C., Ma, J. Z., Pinardi, G., Stavrakou, T., Vlemmix, T., and Van Roozendael,
931 M.: Four years of ground-based MAX-DOAS observations of HONO and NO2 in the
932 Beijing area, Atmospheric Chemistry and Physics, 14, 765-781,
933 10.5194/acp-14-765-2014, 2014.

934 Jethva, H., Torres, O., and Ahn, C.: A ten-year global record of absorbing aerosols
935 above clouds from OMI's near-UV observations, in: Remote Sensing of the
936 Atmosphere, Clouds, and Precipitation Vi, edited by: Im, E., Kumar, R., and Yang, S.,
937 Proceedings of SPIE, 2016.



938 Schenkeveld, V. M. E., Jaross, G., Marchenko, S., Haffner, D., Kleipool, Q. L.,
939 Rozemeijer, N. C., Veefkind, J. P., and Levelt, P. F.: In-flight performance of the
940 Ozone Monitoring Instrument, Atmospheric Measurement Techniques, 10, 1957-1986,
941 10.5194/amt-10-1957-2017, 2017.

942 van Donkelaar, A., Martin, R. V., Spurr, R. J. D., Drury, E., Remer, L. A., Levy, R. C.,
943 and Wang, J.: Optimal estimation for global ground-level fine particulate matter
944 concentrations, Journal of Geophysical Research-Atmospheres, 118, 5621-5636,
945 10.1002/jgrd.50479, 2013.

946 Wang, Y., Lampel, J., Xie, P., Beirle, S., Li, A., Wu, D., and Wagner, T.: Ground-based
947 MAX-DOAS observations of tropospheric aerosols, NO2, SO2 and HCHO in Wuxi,
948 China, from 2011 to 2014, Atmospheric Chemistry and Physics, 17, 2189-2215,
949 10.5194/acp-17-2189-2017, 2017.

Atmos. Meas. Tech. Discuss., https://doi.org/10.5194/amt-2018-34
Manuscript under review for journal Atmos. Meas. Tech.
Discussion started: 7 March 2018


Atmospheric Measurement Techniques Discussions

**Table 1.** Number of CALIOP observations at a grid cell (0.667° × 0.5°).

| | Before filtering | | | | After filtering | | | |
|---|---|---|---|---|---|---|---|---|
| | Mean | Median | Minima | Maximum | Mean | Median | Minima | Maximum |
| For a month | 165 | 169 | 0 | 291 | 47 | 39 | 0 | 223 |
| For the same month in nine years | 1483 | 1513 | 192 | 1921 | 420 | 395 | 0 | 1548 |
| For all months in nine years | 17794 | 18528 | 5608 | 20781 | 5033 | 5381 | 146 | 12650 |

950

Atmos. Meas. Tech. Discuss., https://doi.org/10.5194/amt-2018-34
Manuscript under review for journal Atmos. Meas. Tech.
Discussion started: 7 March 2018


Atmospheric Measurement Techniques Discussions

**Table 2.** MAX-DOAS measurement sites and corresponding meteorological stations.

| MAX-DOAS site name | Site information | Measurement times | Corresponding meteorological station name | Meteorological station information |
|---|---|---|---|---|
| Xianghe | 116.96°E, 39.75°N, 36 m, suburban | 2012/01/01-2012/12/31 | CAPITAL INTERNATIONA | 116.89°E, 40.01°N, 35.4 m |
| IAP | 116.38°E,39.98°N, 92 m, urban | 2008/06/22-2009/04/16 | CAPITAL INTERNATIONA | 116.89°E, 40.01°N, 35.4 m |
| Wuxi | 120.31°E, 31.57°N, 20 m, urban | 2012/01/01-2012/12/31 | HONGQIAO INTL | 121.34°E, 31.20°N, 3 m |

951

Atmos. Meas. Tech. Discuss., https://doi.org/10.5194/amt-2018-34
Manuscript under review for journal Atmos. Meas. Tech.
Discussion started: 7 March 2018


Atmospheric Measurement Techniques Discussions

**Table 3.** Evaluation of OMI $NO_2$ products with respect to MAX-DOAS on 27 haze days [1].

| | POMINO v1.1 | POMINO | DOMINO v2 |
|---|---|---|---|
| Slope | 1.07 | 0.80 | 1.11 |
| Intercept ($10^{15}$ molec./$cm^2$) | -3.58 | 1.76 | -11.79 |
| $R^2$ | 0.76 | 0.68 | 0.38 |
| NMB (%) | 4.4 | -9.4 | -5.0 |

1. The haze days are determined when the ground meteorological station data and MODIS/Aqua corrected reflectance (true color) data both indicate a haze day. Average across the days, AOD = 1.13 (median = 1.10), SSA = 0.90 (0.91), MAX-DOAS $NO_2$ = 51.92 x $10^{15}$ molec. $cm^{-2}$, and CF = 0.06 (0.03).

Atmos. Meas. Tech. Discuss., https://doi.org/10.5194/amt-2018-34
Manuscript under review for journal Atmos. Meas. Tech.
Discussion started: 7 March 2018


Atmospheric Measurement Techniques Discussions

**Table 4.** Evaluation of OMI $NO_2$ products with respect to MAX-DOAS on 36 cloud-free days [1].

| | POMINO v1.1 | POMINO | DOMINO v2 |
|---|---|---|---|
| Slope | 1.30 | 1.13 | 0.92 |
| Intercept ($10^{15}$ molec./$cm^2$) | -0.61 | 0.31 | 2.32 |
| $R^2$ | 0.55 | 0.56 | 0.53 |
| NMB (%) | 29.4 | 20.8 | 21.9 |

1. CF=0 in POMINO product. Average across the days, AOD = 0.60 (median = 0.47), SSA = 0.90 (0.91), and MAX-DOAS $NO_2$ = 26.82 x $10^{15}$ molec. $cm^{-2}$.

Atmos. Meas. Tech. Discuss., https://doi.org/10.5194/amt-2018-34
Manuscript under review for journal Atmos. Meas. Tech.
Discussion started: 7 March 2018


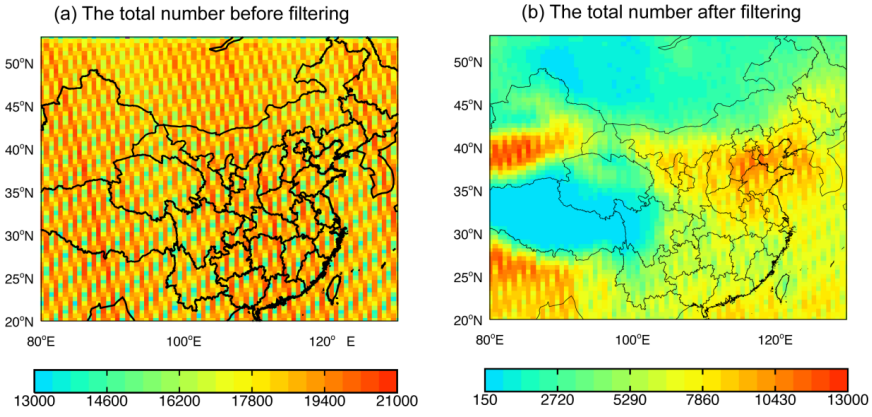


958 Figure 1. The total number of CALIOP Level-2 aerosol extinction profiles at 532 nm
959 used to derive our climatological (2007–2015) dataset on a 0.667° long. x 0.5° lat.
960 grid (a) before and (b) after filtering.

Atmos. Meas. Tech. Discuss., https://doi.org/10.5194/amt-2018-34
Manuscript under review for journal Atmos. Meas. Tech.
Discussion started: 7 March 2018


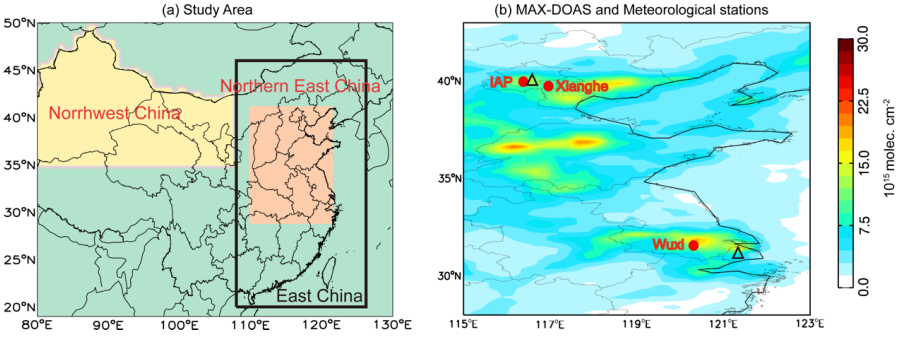


961 Figure 2. (a) Three study areas: Northern East China, Northwest China, and East
962 China. (b) MAX-DOAS measurement sites (red dots) and corresponding
963 meteorological stations (black triangle) overlaid on POMINO v1.1 $NO_2$ VCDs in
964 August 2012.

Atmos. Meas. Tech. Discuss., https://doi.org/10.5194/amt-2018-34
Manuscript under review for journal Atmos. Meas. Tech.
Discussion started: 7 March 2018


Atmospheric Measurement Techniques Discussions

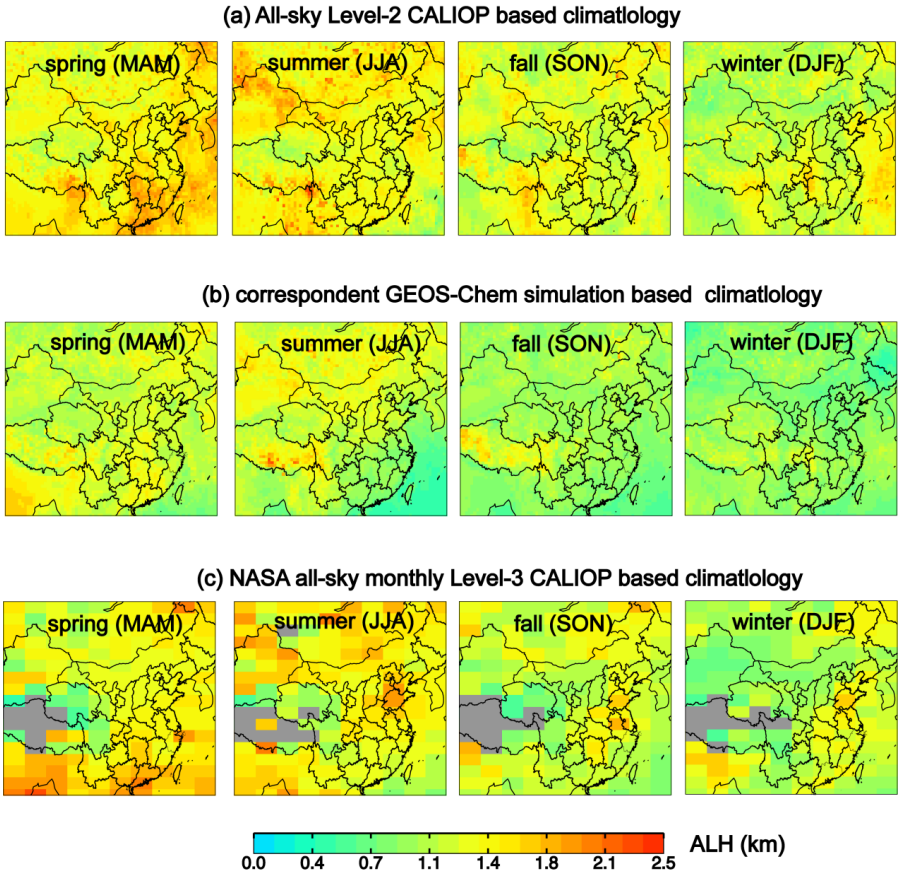


965 Figure 3. Seasonal spatial patterns of ALH climatology at 532 nm on a 0.667° long. x
966 0.50° lat. grid based on (a) our complied all-sky Level-2 CALIOP data, (b)
967 corresponding GEOS-Chem simulations, and (c) NASA all-sky monthly Level-3
968 CALIOP dataset.

Atmos. Meas. Tech. Discuss., https://doi.org/10.5194/amt-2018-34
Manuscript under review for journal Atmos. Meas. Tech.
Discussion started: 7 March 2018


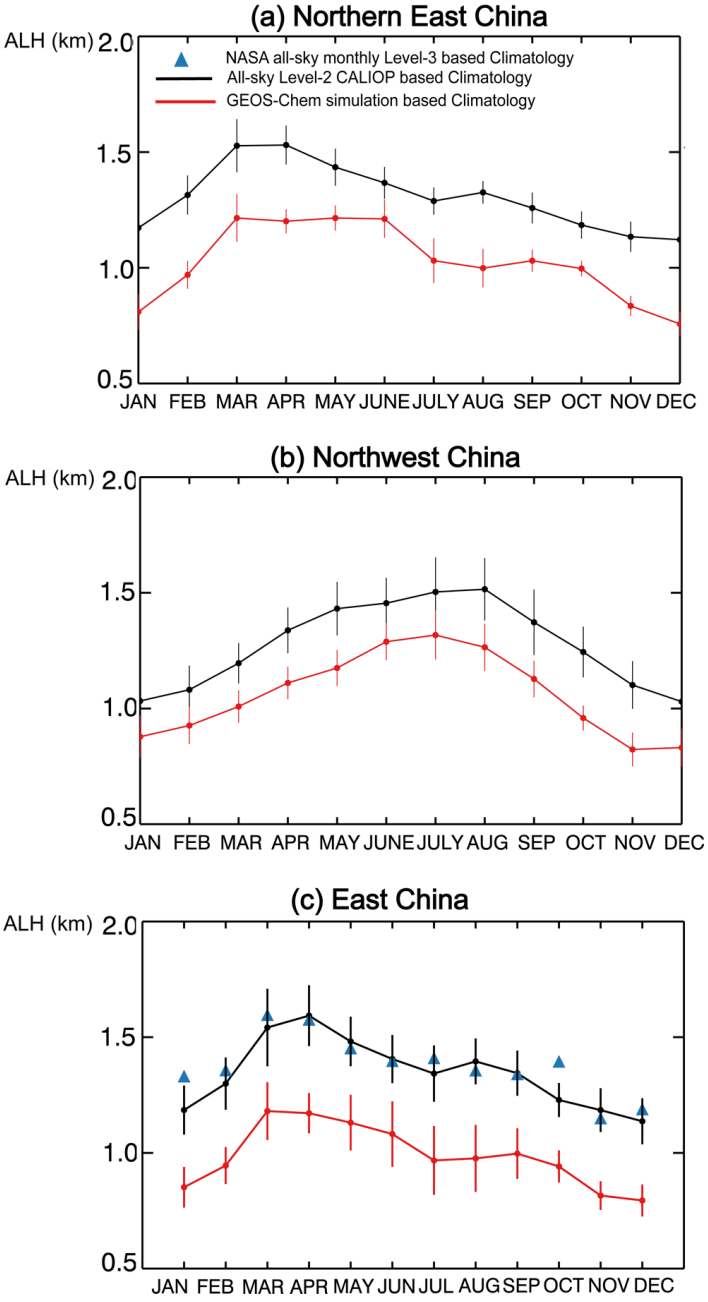


969 Figure 4. Regional mean ALH monthly climatology over (a) Northern East China, (b)
970 Northwest China, and (c) East China. The error bars stand for 1 standard deviation for
971 spatial variability.

972

Atmos. Meas. Tech. Discuss., https://doi.org/10.5194/amt-2018-34
Manuscript under review for journal Atmos. Meas. Tech.
Discussion started: 7 March 2018


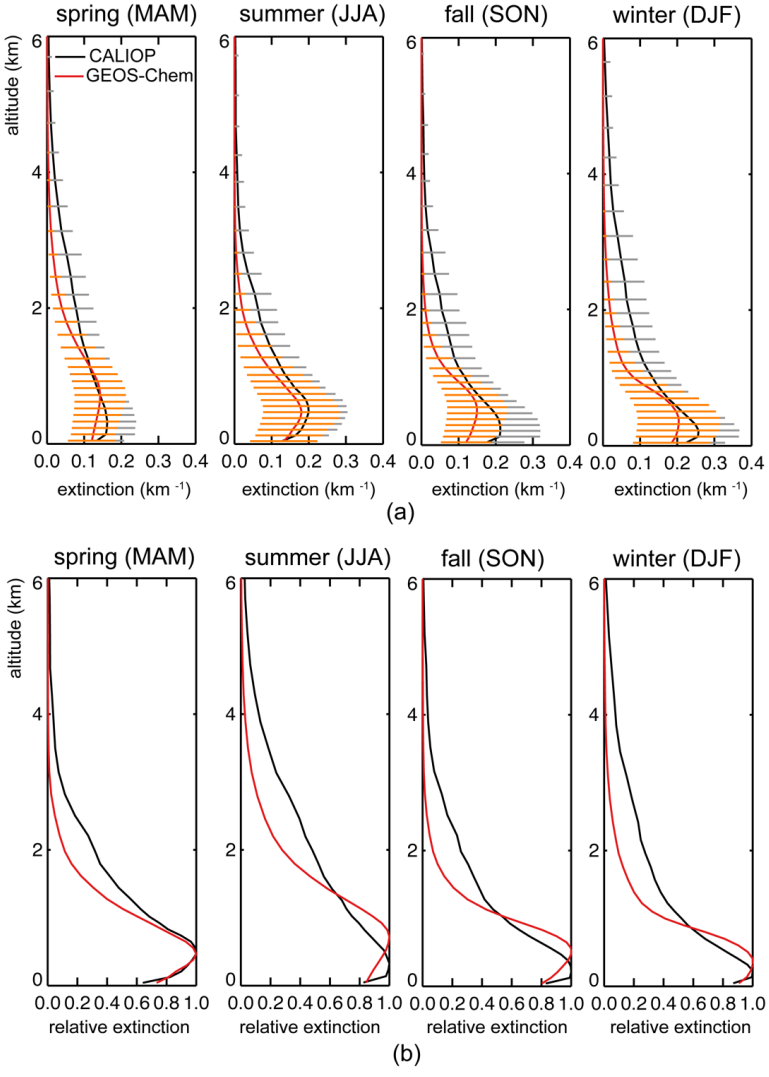


973 Figure 5. Seasonal climatological aerosol extinction profiles (first row) and
974 corresponding relative extinction profiles (normalized to maximum extinction values,
975 second raw) in spring (MAM), summer (JJA), fall (SON) and winter (DJF) over
976 Northern East China. Model results (in red) are prior to MODIS/Aqua based AOD
977 adjustment. Error bars in (a) represent 1 standard deviation across all grid cells in
978 each season.

Atmos. Meas. Tech. Discuss., https://doi.org/10.5194/amt-2018-34
Manuscript under review for journal Atmos. Meas. Tech.
Discussion started: 7 March 2018


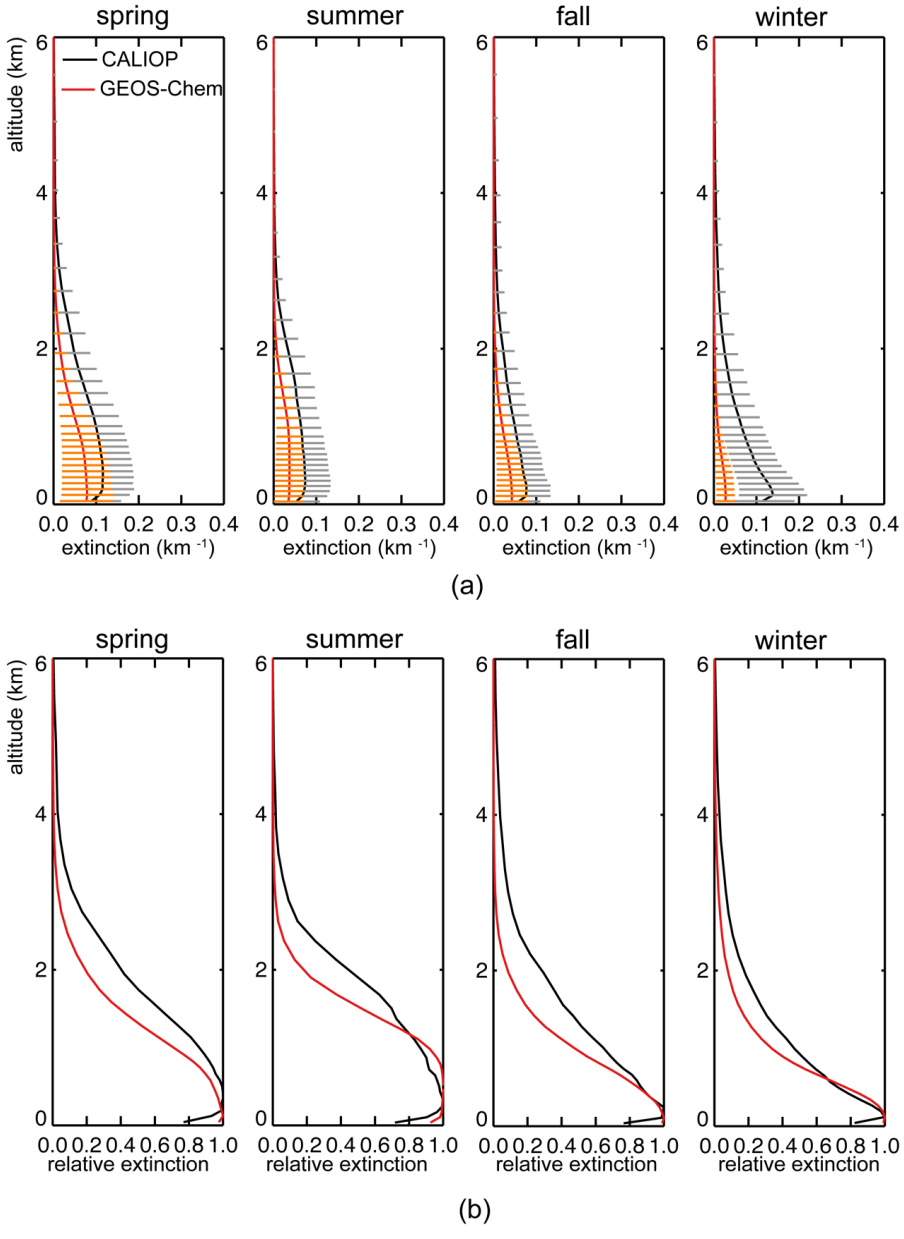


979 Figure 6. Similar to Fig. 5 but for Northwest China.

Atmos. Meas. Tech. Discuss., https://doi.org/10.5194/amt-2018-34
Manuscript under review for journal Atmos. Meas. Tech.
Discussion started: 7 March 2018


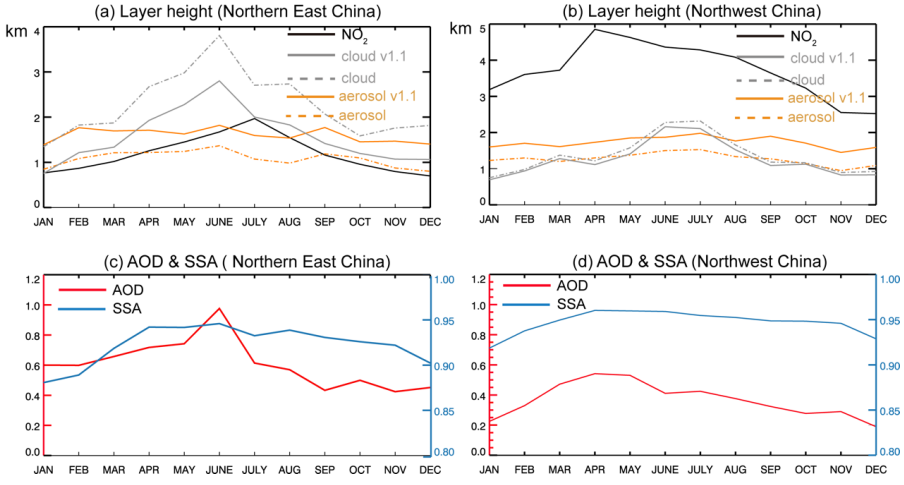


Figure 7. Monthly variations of ALH, CTH and NLH over (a) Northern East China and (b) Northwest China in 2012. Data are averaged across all pixels in each month and region. The grey and orange solid lines denote POMINO v1.1 results, while the corresponding dashed lines denote POMINO. (c–d) Corresponding monthly AOD and SSA.

Atmos. Meas. Tech. Discuss., https://doi.org/10.5194/amt-2018-34
Manuscript under review for journal Atmos. Meas. Tech.
Discussion started: 7 March 2018


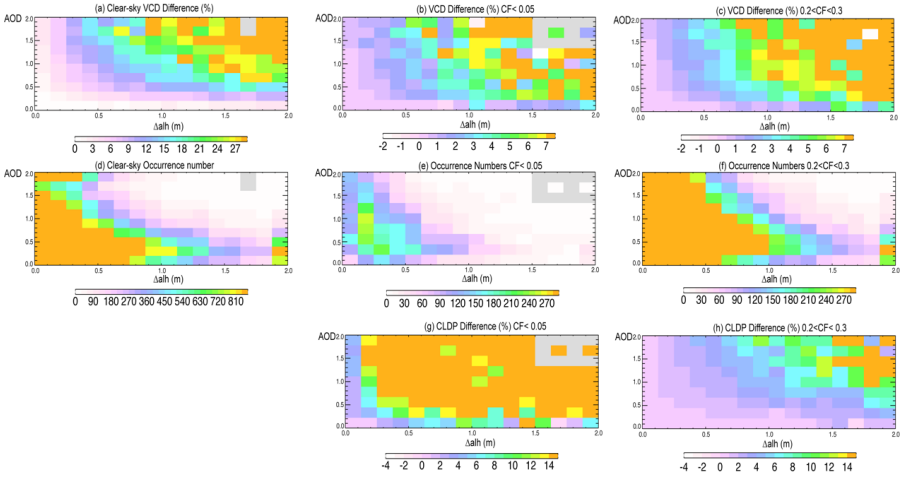


985 Figure 8. Percentage changes in VCD from POMINO to POMINO v1.1 ([POMINO
986 v1.1 – POMINO] / POMINO) for each bin of ΔALH (bin size = 0.2 km) and AOD
987 (bin size = 0.1) across pixels in 2012 over Northern East China, for (a) cloud-free sky
988 (CF = 0 in POMINO), (b) little-cloudy sky, and (c) modestly cloudy sky. (d-f) The
989 number of occurrences corresponding to (a-c). (g, h) Similar to (b, c) but for the
990 percentage changes in cloud top pressure (CP).

Atmos. Meas. Tech. Discuss., https://doi.org/10.5194/amt-2018-34
Manuscript under review for journal Atmos. Meas. Tech.
Discussion started: 7 March 2018


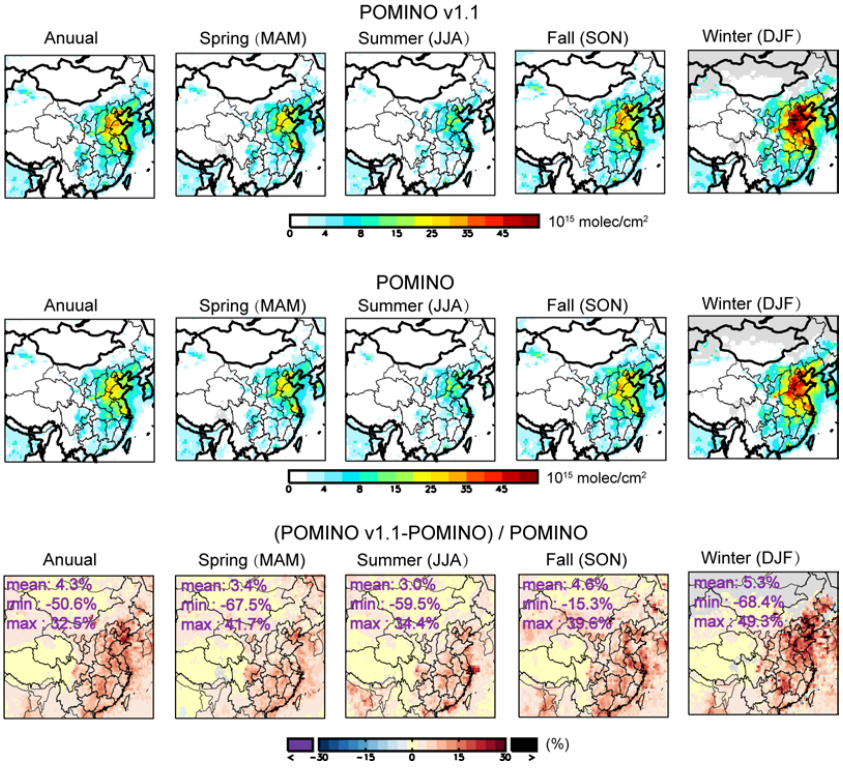


991 Figure 9. Seasonal spatial distribution of tropospheric $NO_2$ VCD in 2012 for (a)
992 POMINO v1.1, (b) POMINO, and (c) their relative difference.

Atmos. Meas. Tech. Discuss., https://doi.org/10.5194/amt-2018-34
Manuscript under review for journal Atmos. Meas. Tech.
Discussion started: 7 March 2018


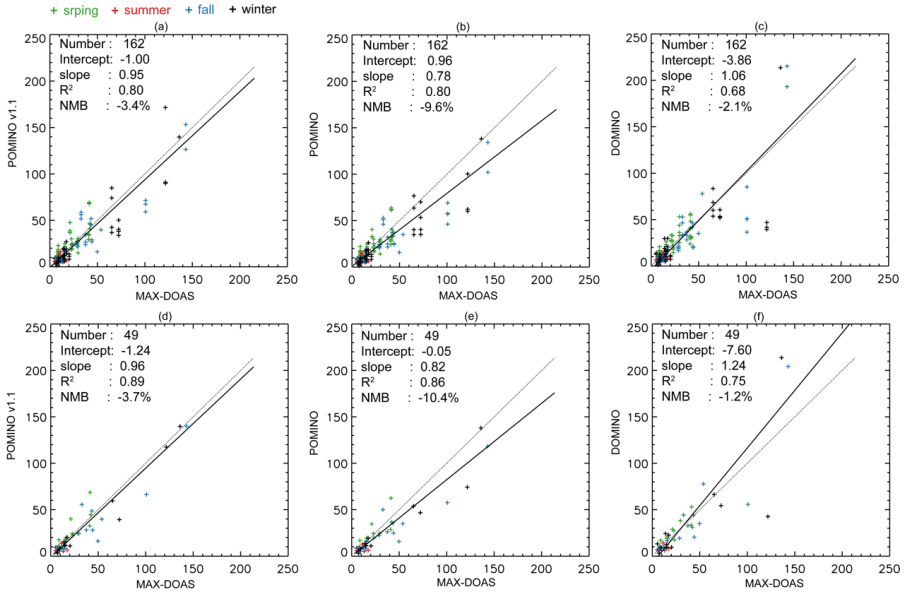


Figure 10. (a–c) Scatterplot for $NO_2$ VCDs ($10^{15}$ molec. $cm^{-2}$) between MAX-DOAS and each of the three OMI products. Each "+" corresponds to an OMI pixel, as several pixels may be available in a day. (d–f) Similar to (a–c) but after averaging over all OMI pixels in the same day, such that each "+" represents a day. Also shown are the statistic results from the RMA regression. The black solid line indicates the regression curve and the grey dotted line depict the 1:1 relationship.